# Long-Lived Long-Distance Photochemically Induced Spin-Polarized Charge Separation in β,β'-Pyrrolic Fused Ferrocene-Porphyrin-Fullerene Systems

*Sai-Ho Lee, Allan G. Larsen, Kei Ohkubo, Zheng-Li Cai , Jeffrey R. Reimers, Shunichi Fukuzumi and Maxwell J. Crossley*

## Electronic Supporting Information

**Table of Contents**

## S1. Experimental and Computational Procedures

### S1.1 General.

Ultraviolet-visible absorption spectra were recorded on a Cary 5E UV-Vis spectrophotometer and NIR-visible absorption spectra were recorded on Shimadzu UV-3100PC in stated solvents. Emission spectra were recorded on a Cary Eclipse Fluorometer in the stated solvents. $^1$H NMR spectra were recorded on a Bruker AVANCE300 (300 MHz) or Bruker DPX400 (400 MHz) spectrometers. Samples were dissolved in deacidified deuterochloroform ($CDCl_3$) containing 0.03 % of tetramethylsilane (TMS) as an internal reference. Electrospray ionization (ESI) and atmospheric pressure chemical ionization (APCI) mass spectrometry were recorded on a ThermoQuest Finnigan LCQ ion trap mass spectrometer equipped with Xcaliber processing software and Hi-resolution ESI mass spectrometry were recorded on a Bruker 7T Fourier Transform Ion Cyclotron Resonance Mass Spectrometer. Infra-red spectra were recorded on a Shimadzu Model 8400 FT-IR as solutions in deacidified chloroform.

### S1.2 Transient Absorption Spectra.

Femtosecond transient absorption spectroscopy experiments were conducted using an ultrafast source: Integra-C (Quantronix Corp.), an optical parametric amplifier: TOPAS (Light Conversion Ltd.) and a commercially available optical detection system: Helios provided by Ultrafast Systems LLC. The source for the pump and probe pulses were derived from the fundamental output of Integra-C (780 nm, 2 mJ/pulse and fwhm = 130 fs) at a repetition rate of 1 kHz. 75% of the fundamental output of the laser was introduced into TOPAS which has optical frequency mixers resulting in tunable range from 285 nm to 1660 nm, while the rest of the output was used for white light generation. Prior to generating the probe continuum, a variable neutral density filter was inserted in the path in order to generate stable continuum, then the laser pulse was fed to a delay line that provides an experimental time window of 3.2 ns with a maximum step resolution of 7 fs. In our experiments, a wavelength between 350 nm to 450 nm of TOPAS output, which are fourth harmonic of signal or idler pulses, was chosen as the pump beam. As this TOPAS output consists of not only desirable wavelength but also unnecessary wavelengths, the latter was deviated using a wedge prism with wedge angle of 18°. The desirable beam was irradiated at the sample cell with a spot size of 1 mm diameter where it was merged with the white probe pulse in a close angle (< 10°). The probe beam after passing through the 2 mm sample cell was focused on a fiber optic cable that was connected to a CCD spectrograph for recording the time-resolved spectra (410–800 nm). Typically, 2500 excitation pulses were averaged for 5 seconds to obtain the transient spectrum at a set delay time. Kinetic traces at appropriate wavelengths were assembled from the time-resolved spectral data. All measurements were conducted at room temperature, 298 K, at porphyrin concentrations of $1.0\times10^{-6}$ M (fs transient spectra and fluorescence spectra).

Spectral components are obtained from the time-dependent spectra by fitting the observed data to the kinetics schemes shown in Schemes 2–4. The total difference spectra $\Delta\varepsilon(t)$ are represented as sums of component spectra $\Delta\varepsilon_i(t)$ weighted by their time-dependent concentrations $C_i$ according to

$$\Delta\varepsilon(t) = \sum_i C_i \Delta\varepsilon_i(t) \qquad \text{(S1)}$$

The concentrations are obtained by solving the kinetics equations given estimated values for the rate constants $k_i$, and optimization yields these rate constants (subsequently presented as the associated lifetimes $\tau_i = 1/k_i$), as well as the spectra of each of the product components. This fitting is done by first smoothing and interpolating the raw experimental data using Gaussian convolution. Prior to fitting, the data is assembled on a linear frequency scale and a logarithmic time scale so as to properly weight the different spectral and temporal regions; the fit is achieved to minimize the residual between the observed and fitted spectra using over-determined linear least-squares analysis to fit the spectral components combined with Newton-Raphson optimization of the rate constants.

For nanosecond laser flash photolysis experiments, deaerated benzonitrile solutions of

porphyrins ($3.0 \times 10^{-6}$ M) were excited by a Panther OPO pumped by Nd:YAG laser (Continuum, SLII-10, 4–6 ns fwhm) at $\lambda = 355$ nm with the power of 16 mJ per pulse. The photochemical reactions were monitored by continuous exposure to a Xe-lamp (150 W) as a probe light and a photomultiplier tube (Hamamatsu 2949) as a detector. For transient absorption spectra in the near-IR region (800–1200 nm), monitoring light from a pulsed Xe-lamp was detected with a Ge-avalanche photodiode (Hamamatsu Photonics, B2834). All experiments were performed at 298 K.

### S1.3 Electrochemical Measurements.

The cyclic voltammetry measurements were performed on a CHI 900B electrochemical analyzer in deaerated benzonitrile containing 0.10 M *n*-$Bu_4NPF_6$ as supporting electrolyte at 298 K. A gold working electrode was polished with BAS polishing alumina suspension and rinsed with acetone before use. The counter electrode was a platinum wire. The measured potentials were recorded with respect to an $Ag/AgNO_3$ (0.01 M) reference electrode, but all experiments were followed by the addition of ferrocene and the ferrocene/ferrocenium redox potentials was used as an internal reference.

### S1.4 EPR Spectroscopy.

The ESR spectra were taken on a JEOL X-band spectrometer (JES-RE1XE) with a quartz ESR tube. The ESR spectrum of charge-separated state of ZnP-$C_{60}$ in frozen PhCN was measured under photoirradiation with a high-pressure mercury lamp (USH–1005D) through a water filter focusing at the sample cell in the ESR cavity at 77–263 K using a liquid nitrogen cryostat before making the spectroscopic measurements. The *g* value was calibrated using an $Mn^{2+}$ marker.

### S1.5 Theory and Computational Modeling.

Density-functional theory (DFT) geometry optimizations for the final charge-transfer state were performed using the B3LYP functional[62,63] with the CEP4G basis[64] for Zn and Fe and the 3-21G basis set[65] for the remaining atoms. While the 3-21G basis set is quite small, B3LYP/3-21G calculations have been shown reproduce many key features in similar systems.[66] All calculations were performed by GASUSSIAN03[67] using a COSMO[68] self-consistent reaction field set to model solvation in benzonitrile. The di-*tert*-butylphenyl groups on the porphyrins were included in all geometry optimizations and DFT energy and excited-state calculations, but these were replaced with H for all vibrational frequency and CASSCF calculations. All non-vibrational calculations involving zinc porphyrins included one coordinated benzonitrile molecule to allow for specific salvation of the chromophore. Energy differences between singlet and triplet states were determined using both time-dependent DFT (TDDFT) and CASSCF methods. CASSCF combined with MP2 perturbation theory (CASPT2) evaluated using MOLPRO[69] was also used for some ferrocenium species.

Electronic couplings $^1V$ for singlet states were determined from the transition moments calculated by TDDFT using Hush's equation[70]

$$^1V = \frac{M}{eR} h\nu \qquad \text{(S2)}$$

where $M$ is the calculated transition moment, $h\nu$ is the calculated transition energy, and $eR$ is the dipole moment of a fully localized transition obtained from the calculated change in the molecular dipole moment component in the direction of electron transfer produced by the excitation.[71] These calculations were performed for neutral molecules in order to determine the coupling for primary charge recombination and secondary charge recombination, while the transition moments for cations or anions were used to model analogous primary and secondary charge-separation processes. All couplings were evaluated at optimized geometries for the charge-separated states in solution.

Spin-orbit couplings linking states on the singlet and triplet manifolds were evaluated at the CASSCF level using GAUSSIAN.[67] The CASSCF calculations included in the active space one virtual orbital of the $C_{60}$ group and two virtual porphyrin orbitals, as well as two occupied orbitals from

porphyrin and two more from ferrocene. As this level of theory is somewhat crude for molecules of the type studied, alternate values for comparison were obtained ad hoc by feeding the molecular-orbital coefficients obtained from B3LYP DFT calculations into the CASSCF property evaluation code; we call this procedure CASDFT. Further, the molecular orbital coefficients were often frozen at their SCF values, reducing the CASSCF program to perform just a simple configuration-interaction (CI) calculation based on a Hartree-Fock ground-state reference; this procedure is called *f*CASSCF. Even with this restriction, CASSCF calculations involving excited ferrocene species are very difficult to perform as the iron *d* orbitals are far too strongly bound at the Hartree-Fock level,[58,72] and for all but the CASPT2 calculations (which properly includes the missing electron correlation), the diagonal one-electron integrals for these orbitals are arbitrarily shifted by -1.45 au so as to produce the same SCF orbital alignment as is calculated naturally using DFT.

Solvent reorganization energies $\lambda_o$ were determined from the differences in the DFT equilibrium and non-equilibrium solvation energies for the ground and triplet excited charge-separated states obtained using a COSMO self-consistent reaction field. A total of four DFT single-point energy calculations are used in this evaluation, one each for the singlet ground state (G) and triplet excited state (E) using the static ($\varepsilon_0$ = 25.2 and infinite-frequency ($\varepsilon_\infty$ = 2.319) dielectric constants of the solvent, yielding the total solvent-solute interaction energies $E_{G0}$, $E_{G\infty}$, $E_{E0}$, and $E_{E\infty}$, Mulliken charges $Q_{G0}$, $Q_{G\infty}$, $Q_{E0}$, and $Q_{E\infty}$, solvent-response charge centres $\mathbf{x}_{G0}$, $\mathbf{x}_{G\infty}$, $\mathbf{x}_{E0}$, and $\mathbf{x}_{E\infty}$, and solvent-response charges $q_{GT}$, $q_{G\infty}$, $q_{E0}$, and $q_{E\infty}$. On vertical excitation, the fraction of the initial-state equilibrium reaction field

$$f = 1 - \frac{\varepsilon_0}{\varepsilon_\infty}\frac{\varepsilon_\infty - 1}{\varepsilon_0 - 1} \tag{S3}$$

originating from the orientational polarization of the solvent is retained and added to the reaction field produced from the infinite-frequency solvent response, giving the reorganization energies for absorption or (charge separation) and emission (or charge recombination) as

$$\lambda_A = E_{E\infty} - E_{E0} - f E_{G0} + f \sum_i \sum_j \frac{Q_{E\infty,i} q_{G0,j}}{\mathbf{x}_i - \mathbf{x}_{G0,j}} \tag{S4}$$

and

$$\lambda_E = E_{G\infty} - E_{G0} - f E_{E0} + f \sum_i \sum_j \frac{Q_{G\infty,i}\, q_{E0,j}}{|\, \mathbf{x}_i - \mathbf{x}_{E0,j}\,|} \tag{S5}$$

respectively, where $\mathbf{x}_i$ are the atomic coordinates. In most cases the absorption and emission reorganization energies are very similar and only the average values $\lambda_o$ are reported in the results tables. These equations reduce to the standard Marcus equation[73]

$$\lambda_o = \frac{1}{2}\left(\frac{1}{R_D} + \frac{1}{R_A} - \frac{2}{R}\right)\left(\frac{1}{\varepsilon_\infty} - \frac{1}{\varepsilon_0}\right) \tag{S6}$$

for the case where the donor and acceptor groups can be represented as solvated charges inside spherical solvent cavities of radius $R_D$ and $R_A$ separated a distance $R$. One technical difficulty with these calculations is a propensity for the solvent charges not to converge owing to the intricate molecular shapes involved. To obtain robust results, the solvent-accessible surface was used with a solvent radius of 0.5 Å. Compared to the default solvent-excluded surface (i.e, zero solvent radius), the calculated reorganization energies are systematically reduced by ca. 10%.

The internal reorganization energy of each porphyrin, fullerene, or ferrocene fragment was determined following geometry optimization of the fragment in its neutral and charged states using B3LYP. Vibrational displacements associated with each redox process were then evaluated by projecting the coordinate displacement onto the normal modes of the neutral species using curvilinear

coordinates.[74] These intramolecular reorganization energies and associated Franck-Condon factors were used in the fitting of couplings $V$ and solvent reorganization energies $\lambda_o$ to observed kinetic data using the semiclassical rate expression:[61]

$$k = \frac{2\pi V^2}{\hbar(4\pi\lambda_0 k_\beta T)^{1/2}} \sum_n P_n \sum_m \exp\frac{-(\Delta G^0 + E_m - E_n + \lambda_o)^2}{4\lambda_o k_\beta T} < \chi_n \mid \chi_m >^2 \qquad \text{(S7)}$$

where $T$ is the temperature, $k_\beta$ is Boltzmann's constant, $n$ and $m$ are quantum-number sets indexing the vibrational levels of the initial and final states of energy $E_n$ and $E_m$ with wavefunction $|\chi_n>$ and $|\chi_m>$, respectively, and $P_n$ is the probability of thermal vibrational excitation on the initial state,

$$P_n = \frac{\exp(-E_n / k_\beta T)}{\sum_k \exp(-E_k / k_\beta T)} \qquad \text{(S8)}$$

## S2. Synthetic Details and Characterization.

**S2.1 ZnP**, **2HP**, **ZnP-Ph**, **2HP-Ph**, **ZnP-$C_{60}$**, **2HP-$C_{60}$** and **Fc-ZnP-$C_{60}$L** were prepared following the methods developed earlier in our laboratory.[34,35,43,44]

**S2.2 Ferrocene-nitro-(zinc porphyrin) 2.** Nitroporphyrin-dione[38] **1** (1.0 g, 0.83 mmol), ferrocene-carboxaldehyde (217.0 mg, 1.01 mmol) and ammonium acetate (390.0 mg, 5.06 mmol) were dissolved in $CHCl_3$/AcOH (5:1, 180 mL). The reaction mixture was heated at reflux, in the dark, for 4 h. The solvent was removed under reduced pressure and the residue was purified by column chromatography over silica ($CH_2Cl_2$/hexane; 2:1). The major band was collected and recrystallized from a mixture of $CH_2Cl_2$/MeOH to yield ferrocene-nitroporphyrin **2** (885.0 mg, 76%). UV-vis ($CHCl_3$) 427 (log $\varepsilon$ 5.51), 524 (4.07), 555 (4.29), 601 (4.48) nm. $^1$H NMR (300 MHz, $CDCl_3$) $\delta$ ppm 1.53 (s, 36H), 1.57 (s, 36H), 4.08 (s, 5H), 4.40 (t, $J$ = 1.9 Hz, 2H), 4.66 (t, $J$ = 1.9 Hz, 2H), 7.61 (s, 1H), 7.81–7.82 (m, 2H), 7.88 (s, 1H), 8.03–8.11 (m, 9H), 8.92–9.04 (m, 4H), 9.24 (s, 1H). ESI-MS (*m/z*): $[M + H]^+$ 1395.07 obtained.

**S2.3 Ferrocene-zinc porphyrin-dione 3.** Ferrocene-nitroporphyrin **2** (885.0 mg, 0.63 mmol) and tin(II) chloride dihydrate (375.0 mg, 1.66 mmol) were dissolved in HCl/$Et_2O$ (100 mL) and stirred, in the dark, for 20 h. The solution was passed through a silica plug and the solvent was removed under reduced pressure. The residue was dissolved in $CH_2Cl_2$ (800 mL) and Rose Bengal (5 mg) was added. The reaction mixture was photo-oxidized for 1 h, and the solvent was removed under reduced pressure. The residue was redissolved in $CH_2Cl_2$ (200 mL) and HCl (2 M, 200 mL) was added and stirred vigorously for 30 min. The solvent was removed under reduced pressure and the residue was purified by column chromatography over silica ($CH_2Cl_2$/hexane; 2:1). The major fraction was separated and the solvent was removed under reduced pressure. The residue was redissolved in $CH_2Cl_2$/MeOH (10:1, 110 mL). Zinc(II) acetate dihydrate (300.0 mg, 1.37 mmol) was added and the solution was stirred at room temperature for 2 h. The reaction mixture was passed through a silica plug and the solvent was removed under reduced pressure. The residue was purified by column chromatography over silica ($CH_2Cl_2$). The first green band was collected and recrystallized from a mixture of $CH_2Cl_2$/MeOH to yield ferrocene-nitroporphyrin **2** (21.0 mg, 2%). The second red band yielded ferrocene-porphyrin-dione **3** (142.0 mg, 17%). UV-vis ($CHCl_3$) 411 (log ε 5.40), 494 (4.66), 514 (4.55), 631 (4.28) nm. IR ($CHCl_3$) ν 1722 (s, CO stretch), 3433 (m, imidazole NH stretch) $cm^{-1}$. $^1$H NMR (300 MHz, $CDCl_3$) δ ppm 1.46 (s, 18H), 1.48 (s, 18H), 1.51 (s, 18H), 1.52 (s, 18H), 4.04 (s, 5H), 4.36 (t, $J$ = 1.9 Hz, 2H), 4.56 (t, $J$ = 1.9 Hz, 2H), 7.53 (br s, 1H), 7.64 (d, $J$ = 1.7 Hz, 2H), 7.70 (t, $J$ = 1.7 Hz, 1H), 7.73(d, $J$ = 1.7 Hz, 3H), 7.81 (br s, 1H), 7.92 (m, 4H), 7.96 (br s, 1H), 8.26 (d, $J$ = 4.7 Hz, 1H), 8.44 (d, $J$ = 4.7 Hz, 1H), 8.49 (d, $J$ = 4.7, 1H), 8.52 (d, $J$ = 4.7, 1H). ESI-MS (*m/z*): $[M + H]^+$ 1380.00 obtained, $[M + MeOH]^+$ 1414.07 obtained.

**S2.4 Ferrocene-porphyrinoimidazole-benzaldehyde 4.** Ferrocene-porphyrin-dione **3** (100.0 mg, 0.07 mmol) was dissolved in $CHCl_3$/AcOH (5:1, 30 mL) and terephthaldicarboxaldehyde (100.0 mg, 0.75 mmol) and ammonium acetate (30.0 mg, 0.39 mmol) were added. The reaction mixture was heated at reflux, in the dark, for 2.5 h. The solvent was removed under reduced pressure and the residue was purified by column chromatography over silica ($CH_2Cl_2$/EtOAc; 20:1). The major fraction was collected and recrystallized from a mixture of $CH_2Cl_2$/MeOH to give ferrocene-porphyrinoimidazole-benzaldehyde **4** (37.0 mg, 34%). UV-vis ($CHCl_3$) 427 (log ε 5.46), 547 (4.56), 582 (3.92) nm. IR ($CHCl_3$) ν 1701 (s, CO stretch), 3437 (m, imidazole NH stretch) $cm^{-1}$. $^1H$ NMR (300 MHz, $CDCl_3$) δ ppm 1.54 (s, 48H), 1.58 (s, 24H), 4.10 (s, 5H), 4.41 (t, $J$ = 1.9 Hz, 2H), 4.73 (t, $J$ = 1.9 Hz, 2H), 7.49–7.62 (m, 1H), 7.81 (s, 1H), 7.88–8.03 (m, 5H), 8.06–8.24 (m, 10H), 8.58–8.65 (m, 1H), 8.93–9.07 (m, 4H), 10.06 (s, 1H). ESI-MS (*m/z*): $[M + H]^+$ 1495.87 obtained.

**S2.5 Corner ferrocene-(zinc porphyrin)-fullerene triad Fc-ZnP-$C_{60}$C.** Ferrocene-porphyrinoimidazole-benzaldehyde **4** (30.0 mg, 0.02 mmol), fullerene (22.0 mg, 0.03 mmol) and sarcosine (18.0 mg, 0.20 mmol) were dissolved in dry toluene (15 mL). The reaction mixture was heated at reflux, in the dark, under nitrogen for 20 h. The solvent was removed under reduced pressure. The crude product was purified by column chromatography over silica ($CH_2Cl_2$). The major red band was collected and recrystallized from a mixture of $CH_2Cl_2$/MeOH to give corner ferrocene-(zinc porphyrin)-fullerene **Fc-ZnP-$C_{60}$C** (35.0 mg, 78%). UV-vis (PhCN) 435 (log ε 5.32), 513sh (3.65), 557 (4.32), 592 (3.55) nm. $^1H$ NMR (400 MHz, $CDCl_3$) δ ppm 1.45–1.58 (m, 72H), 2.60 (s, 3H), 3.59 (m, 1H), 4.06 (d, $J$ = 5.6 Hz, 5H), 4.29 (m, 1H), 4.41 (s, 2H), 4.62 (s, 1H), 4.74 (s, 2H), 7.46–7.80 (m, 6H), 8.01–8.20 (m, 11H), 8.48 (d, $J$ = 7.3 Hz, 1H), 8.93–9.03 (m, 4H). ESI-MS (*m/z*): $[M + H]^+$ 2242.38 obtained. HR-ESI-MS (m/z): $C_{157}H_{111}ZnFeN_9$ $[M + H]^+$ 2243.76606 calculated, 2243.79511 obtained; $[M + 2H]^{2+}$ 1121.88275 calculated, 1121.88381 obtained.

**S2.6 Ferrocene-(zinc porphyrin) dyad Fc-ZnP.** Zinc porphyrin-dione (100 mg, 0.09 mmol), ferrocenecarboxaldehyde (20 mg, 0.09 mmol) and ammonium acetate (340 mg, 4.41 mmol) were dissolved in $CHCl_3$/AcOH (9:1, 200 mL). The reaction mixture was heated at reflux, in the dark, for 3 h. The solvent was removed under reduced pressure and the residue was purified by column chromatography over silica ($CH_2Cl_2$/hexane; 2:1). The major red band was collected and recrystallized from a mixture of $CH_2Cl_2$/MeOH to yield ferrocene-(zinc porphyrin) **Fc-ZnP** (52 mg, 45%). UV-vis (PhCN) 432 (log ε 5.56), 521 (3.90), 560 (4.31), 600 (4.15) nm. $^1H$ NMR (300 MHz, $CDCl_3$) δ ppm 1.54 (s, 36H), 1.58 (s, 36H), 4.11 (s, 5H), 4.44 (t, $J$ = 1.9 Hz, 2H), 4.70 (t, $J$ = 1.9 Hz, 2H), 7.81 (s, 2H), 7.88 (t, $J$ = 1.9 Hz, 1H), 8.07 (t, $J$ = 1.9 Hz, 1H), 8.14 (d, $J$ = 2.3 Hz, 6H), 8.16 (d, $J$ = 1.3 Hz, 2H), 8.21 (s, 1H), 8.99–9.09 (m, 6H). ESI-MS (*m/z*): $[M + H]^+$ 1350.13 obtained. HR-ESI-MS (m/z): $C_{87}H_{101}N_6FeZn$ $[M + H]^+$ 1351.67370 calculated, 1351.67231 obtained.

**S2.7 Ferrocene-(free-base porphyrin) dyad Fc-2HP. Fc-2HP** was prepared by the demetalation of **Fc-ZnP** (68 mg, 0.05 mmol) using hydrochloric acid (5 M). The product was purified by column chromatography over silica ($CH_2Cl_2$/hexane; 2:1). The major band was collected and recrystallized from a mixture of $CH_2Cl_2$/MeOH to yield ferrocene-(free-base porphyrin) **Fc-2HP** (52 mg, 80%). UV-vis (PhCN) 424 (log ε 5.42), 522 (4.25), 553 (3.95), 592 (3.82) 652 (3.72) nm. $^1H$ NMR (300 MHz, $CDCl_3$) δ ppm -2.81 (s, 2H), 1.53 (s, 36H), 1.57 (s, 18H), 1.60(s, 18H), 4.09 (s, 5H), 4.38 (t, $J$ = 1.9 Hz, 2H), 4.67 (t, $J$ = 1.9 Hz, 2H), 7.80 (t, $J$ = 1.9 Hz, 2H), 7.86 (t, $J$ = 1.9 Hz, 1H), 8.07 (d, $J$ = 1.7 Hz, 2H), 8.11–8.13 (m, 4H), 8.16 (d, $J$ = 1.7 Hz, 2H), 8.84–9.00 (m, 6H). ESI-MS (*m/z*): $[M + H]^+$ 1288.20 obtained. HR-ESI-MS (m/z): $C_{87}H_{103}N_6Fe$ $[M + H]^+$ 1287.75913 calculated, 1287.75733 obtained.

**S2.8 3,5-Di-*tert*-butylphenyl N-methylfulleropyrrolidine Ph-$C_{60}$.** 3,5-di-*tert*-butylphenyl N-methylfulleropyrrolidine **Ph-$C_{60}$** was prepared according to an established method.[75] 3,5-Di-*tert*-butylbenzaldehyde (30 mg, 0.14 mmol), fullerene (100 mg, 0.14 mmol) and sarcosine (62.0 mg, 0.70 mmol) were dissolved in dry toluene (20 mL). The reaction mixture was heated at reflux, in the dark, under nitrogen for 20 h. The solvent was removed under reduced pressure. The crude product was purified by column chromatography over silica (hexane/toluene; 1:1). The major fraction was collected

and recrystallized from a mixture of toluene/MeOH to yield 3,5-di-*tert*-butylphenyl N-methylfulleropyrrolidine **Ph-$C_{60}$** (33 mg, 25%). UV-vis (PhCN) 354 (log $\varepsilon$ 4.32), 432 (3.70), 707 (2.69) nm. $^1$H NMR (300 MHz, $d_8$-toluene) δ ppm 1.31 (s, 18H), 2.65 (s, 3H), 3.88 (d, $J$ = 9.4 Hz, 1H), 4.53 (d, $J$ = 9.4 Hz, 1H), 4.76 (s, 1H), 7.43 (m, 1H), 7.58–8.00 (br, 2H). APCI-MS (m/z): $[M + H]^+$ 966.47 obtained.

**S2.9 bis(ferrocenyl)-porphyrin Fc-ZnP-Fc.** Corner zinc(II) porphyrin-tetraone[44] (154 mg, 130 μmol), ferrocenecarboxaldehyde (24.0 mg, 110 μmol) and ammonium acetate (500 mg, 6.49 mmol) were dissolved in a mixture of chloroform/acetate acid (9:1, 50 mL) and heated at reflux for 6 h. The reaction mixture was allowed to cool to room temperature, then washed with water (3 × 50 mL), sodium carbonate solution (5%, 50 mL), then dried over anhydrous sodium sulfate. The solvent was removed and the residue was purified by chromatography over silica (dichloromethane). The major green band yielded unreacted corner zinc(II) porphyrin-tetraone. Then, the polarity was increased (dichloromethane/ethyl acetate; 20:1) and the major red-brown band yielded corner zinc(II) bis(ferrocenyl)porphyrin **F –ZnP-Fc** (54.0 mg, 62%). UV-vis ($CHCl_3$) 421 (log ε 5.31), 546 (4.30), 582 (3.85) nm. $^1$H NMR (300 MHz, $CDCl_3$) δ 1.54 (s, 18H, *tert*-butyl H), 1.58 (s, 36 H, *tert*-butyl H), 1.62 (s, 18H, *tert*-butyl H), 4.10 (s, 5H, Fc), 4.11 (s, 5H, Fc), 4.40 (t, $J$ = 1.7 Hz, 4H, Fc), 4.70 (t, $J$ = 1.7 Hz, 2H, Fc), 4.72 (t, $J$ = 1.7 Hz, 2H, Fc), 7.79-7.80 (m, 1H), 7.87, (br s, 1H), 8.05 (m, 1H), 8.14 (b, $J$ = 1.5 Hz, 5H), 8.18 (d, $J$ = 1.5 Hz, 2H), 8.22 (d, $J$ = 1.5 Hz, 2H), 8.25 (br s, 2H), 8.95-8.98 (dd, $J$ = 2.2, 4.5 Hz, 2H, β-pyrrolic H), 9.01-9.03 (d, $J$ = 4.5 Hz, 1H, β-pyrrolic H), 9.05-9.06 (d, $J$ = 4.5 Hz, 1H, β-pyrrolic H). ESI-MS (*m/z*): $[M + H]^+$ 1575.80 obtained.

## S3. Results

### S3.1. Electrochemistry.

Figures S1–S9 show the observed cyclic voltammograms for the compounds whose redox data are summarized in Table 1 of the main text.

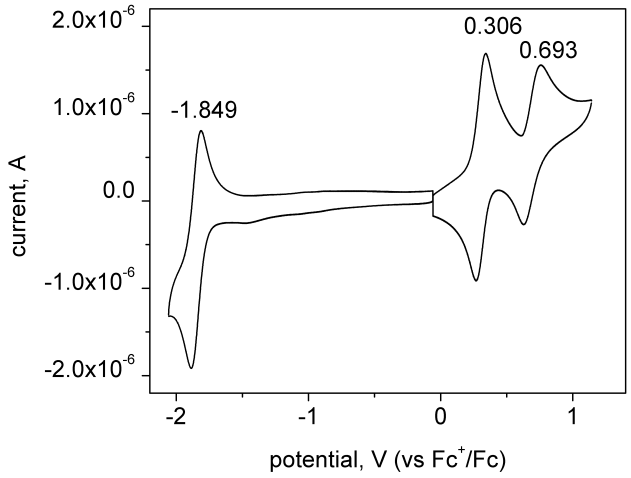


**Fig. S1** Cyclic voltammograms of **ZnP** (1.0 mM) in deaerated PhCN containing 0.10 M *n*-$Bu_4NPF_6$ at 298 K.

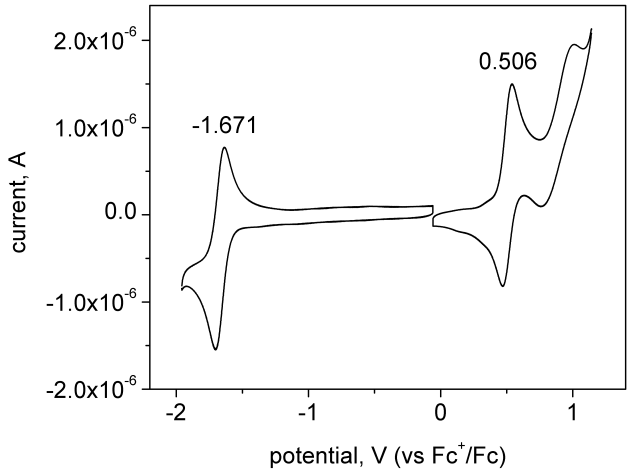


**Fig. S2** Cyclic voltammograms of **2HP** (1.0 mM) in deaerated PhCN containing 0.10 M *n*-$Bu_4NPF_6$ at 298 K.

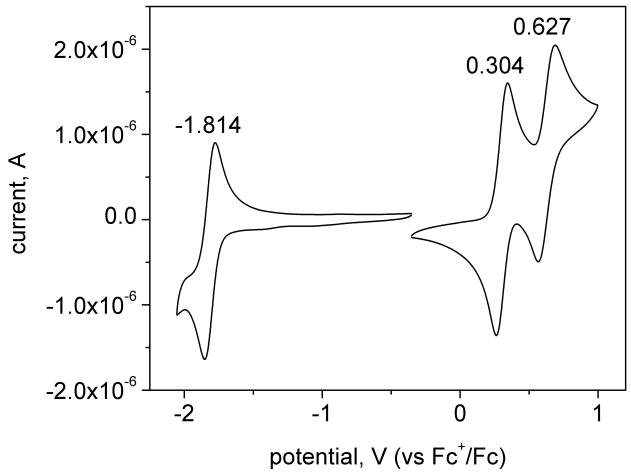


**Fig. S3** Cyclic voltammograms of **ZnP-Ph** (1.0 mM) in deaerated PhCN containing 0.10 M *n*-$Bu_4NPF_6$ at 298 K.

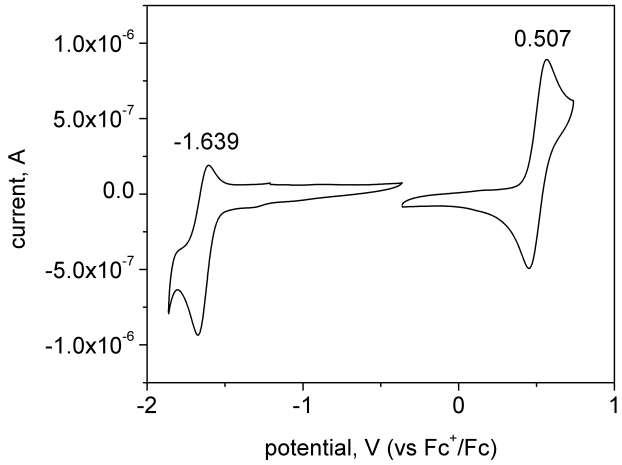


**Fig. S4** Cyclic voltammograms of **2HP-Ph** (1.0 mM) in deaerated PhCN containing 0.10 M *n*-$Bu_4NPF_6$ at 298 K.

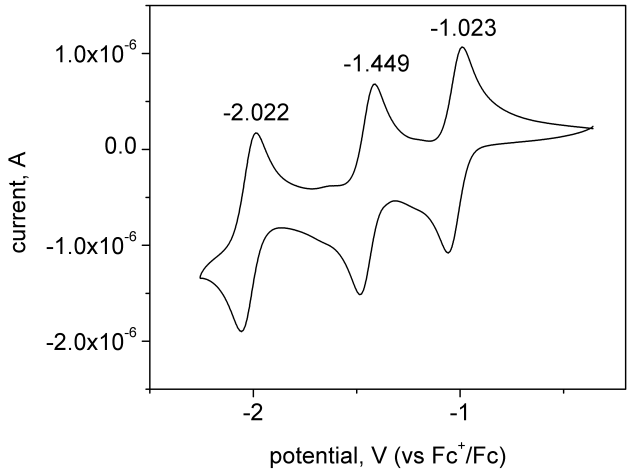


**Fig. S5** Cyclic voltammogram of **Ph-$C_{60}$** (1.0 mM) in deaerated PhCN containing 0.10 M *n*-$Bu_4NPF_6$ at 298 K.

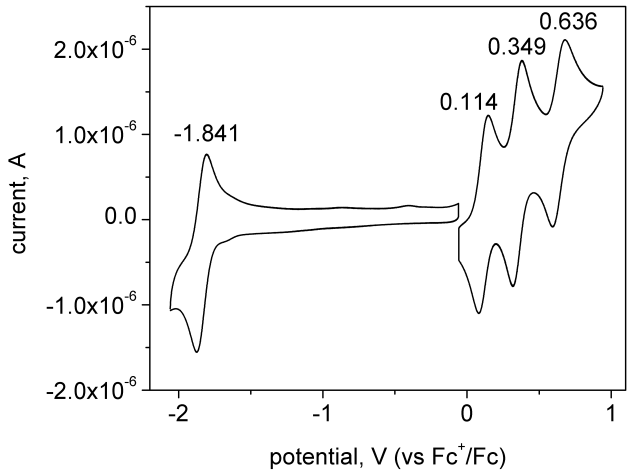


**Fig. S6** Cyclic voltammograms of **Fc-ZnP** (1.0 mM) in deaerated PhCN containing 0.10 M *n*-$Bu_4NPF_6$ at 298 K.

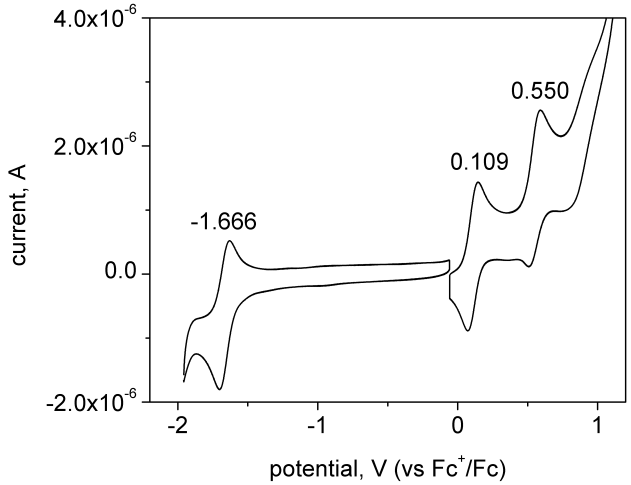


**Fig. S7** Cyclic voltammograms of **Fc-2HP** (1.0 mM) in deaerated PhCN containing 0.10 M *n*-$Bu_4NPF_6$ at 298 K.

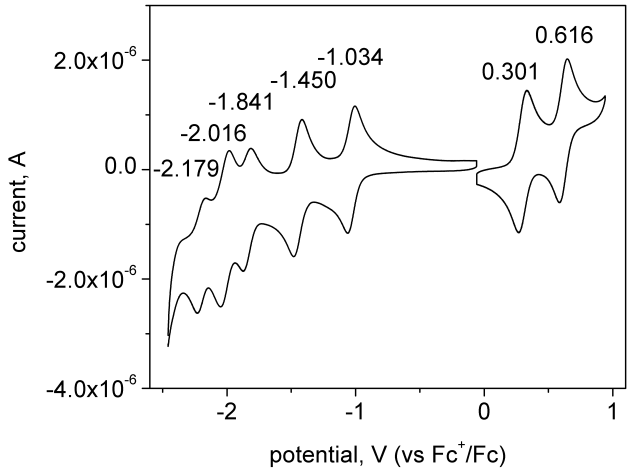


**Fig. S8** Cyclic voltammogram of **ZnP-$C_{60}$** (1.0 mM) in deaerated PhCN containing 0.10 M *n*-$Bu_4NPF_6$ at 298 K.

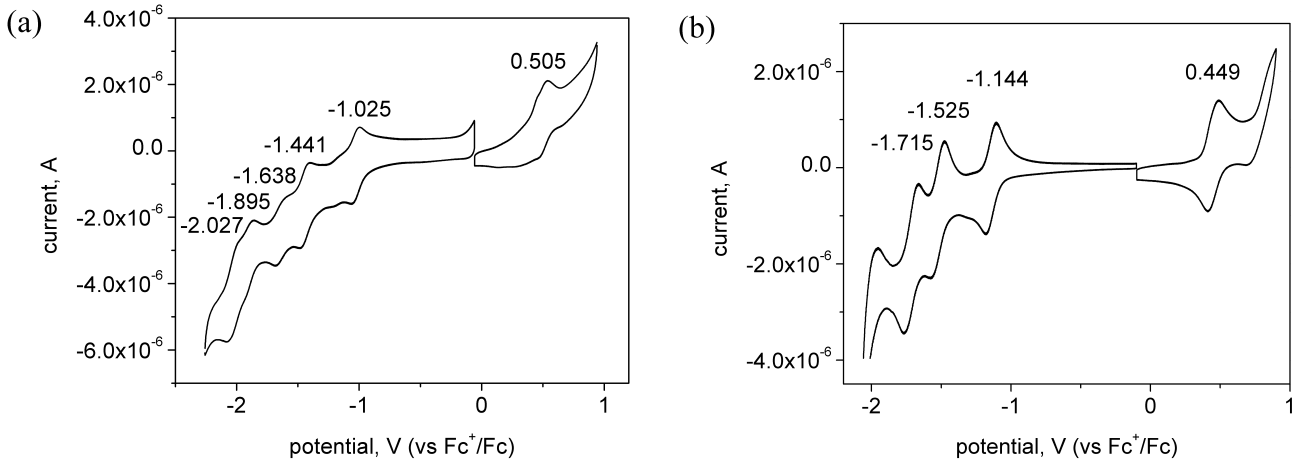


**Fig. S9** Cyclic voltammograms of **2HP-C$_{60}$** (1.0 mM) in deaerated (a) PhCN; and (b) $CH_2Cl_2$ containing 0.10 M *n*-$Bu_4NPF_6$ at 298 K.

**Table S1** Free-energy changes $\Delta G$ (eV) for electron-transfer reactions in PhCN calculated from the electrochemical potentials after correction for the Coulomb interaction between the charges[a]

| Reaction | seq.[b] | $^1CS_1$ | $^3CS_1$[c] | $^{1,3}CR_1$ | $^{1,3}CS_2$ | $^{1,3}CR_2$ |
|---|---|---|---|---|---|---|
| Fc-ZnP$^*$ → Fc$^{\bullet+}$-ZnP$^{\bullet-}$ | - | -0.18 | 0.35 | -1.88 | - | - |
| Fc-2HP$^*$ → Fc$^{\bullet+}$-2HP$^{\bullet-}$ | - | -0.20 | 0.33 | -1.70 | - | - |
| ZnP$^*$-$C_{60}$ → ZnP$^{\bullet+}$-$C_{60}^{\bullet-}$ | - | -0.76 | -0.19 | -1.30 | - | - |
| 2HP$^*$-$C_{60}$ → 2HP$^{\bullet+}$-$C_{60}^{\bullet-}$ | - | -0.29 | 0.24 | -1.61 | - | - |
| Fc-ZnP$^*$-$C_{60}$L → Fc-ZnP$^{\bullet+}$-$C_{60}^{\bullet-}$L → Fc$^{\bullet+}$-ZnP-$C_{60}^{\bullet-}$L | a | -0.72 | -0.20 | -1.33 | -0.20 | -1.13 |
| Fc-ZnP$^*$-$C_{60}$L → Fc$^{\bullet+}$-ZnP$^{\bullet-}$-$C_{60}$L → Fc$^{\bullet+}$-ZnP-$C_{60}^{\bullet-}$L | b | 0.01 | 0.53 | -2.06 | -0.93 | -1.13 |
| Fc-ZnP$^*$-$C_{60}$C → Fc-ZnP$^{\bullet+}$-$C_{60}^{\bullet-}$C → Fc$^{\bullet+}$-ZnP-$C_{60}^{\bullet-}$C | a | -0.76 | -0.20 | -1.32 | -0.20 | -1.12 |
| Fc-ZnP$^*$-$C_{60}$C → Fc$^{\bullet+}$-ZnP$^{\bullet-}$-$C_{60}$C → Fc$^{\bullet+}$-ZnP-$C_{60}^{\bullet-}$C | b | -0.02 | 0.53 | -2.06 | -0.94 | -1.12 |

[a] The initially excited porphyrin may be either P$^*$ = $^1P(S_1)^*$ or $^1P(T_1)^*$ leading to different energies for primary charge separation within the singlet and triplet state manifolds; the differences between the energies of the singlet and triplet $CR_1$, $CS_2$, and $CR_2$ processes are insignificant (< 0.001 eV), however. $\Delta G_{CR1} = E°$(anion red.) – $E°$(cation ox.) + $e/4\pi\varepsilon_0\varepsilon_s R$ is for charge-recombination from the primary charge-separated state where $R$ is the charge separation distance determined from DFT; $\Delta G_{CS1} = -\Delta G_{CR1} - \Delta E_{0\text{-}0}$ is the free energy change for primary charge-separation where $\Delta E_{0\text{-}0}$ is the energy of the lowest excited state calculated as the average of the energy of the (0-0) band in the absorption and the emission spectra; $\Delta G_{CS2} = E°$(new group ox.) – $E°$(old group ox.) + $(e/4\pi\varepsilon_0\varepsilon_s)(1/R_{old} - 1/R_{new})$ is the free energy change for secondary charge-separation where $R_{old}$ is the distance from the counter ion to the originally charged group and $R_{new}$ is the distance from the counter ion to the newly charged group; and $\Delta G_{CR2} = \Delta G_{CR1} - \Delta G_{CS2} = E^0$(final anion red.) - $E_{1/2}$(final cation ox.) + $1/\varepsilon_0 R$ is the free energy change for the charge-recombination from the fully charge-separated state. The parameters used are: $\varepsilon_0 = 25.2$ for PhCN, $R_{P\text{-}Fc} = 9$ Å, $R_{C60\text{-}P} = 14$ Å, $R_{C60\text{-}Fc} = 23$ Å (for **Fc-ZnP-C$_{60}$L**) or 16 Å (for **Fc-ZnP-C$_{60}$C**), with the distances taken from the DFT optimized structures..

[b] For the triads, two sequences of charge separation processes are possible.

[c] Estimated using the singlet-triplet splitting of 0.53 eV measured for **ZnP-C$_{60}$**.

### S3.2 Time-resolved fluorescence spectroscopy

Figures S10 and S11 show the observed time-resolved fluorescence of the model compounds **ZnP** and **2HP**, respectively. The fluorescence lifetimes listed in Table 2 of the main text are fitted to the long-time decaying parts of the fluorescence profiles.

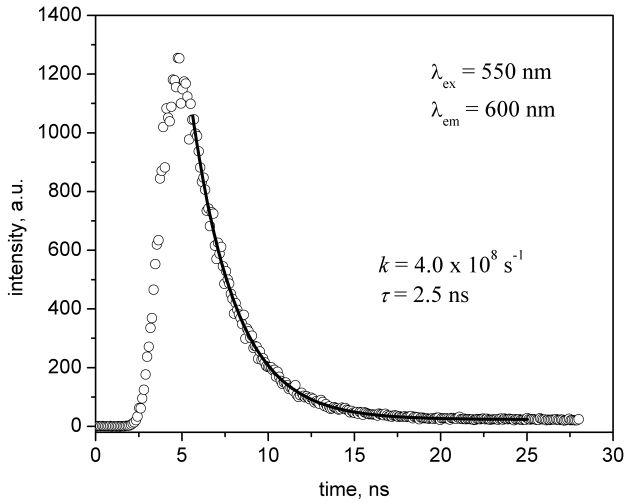


**Fig. S10** The time-decay profile of **ZnP** ($8.6 \times 10^{-6}$ M) in PhCN measured by time-resolved fluorescence spectroscopy.

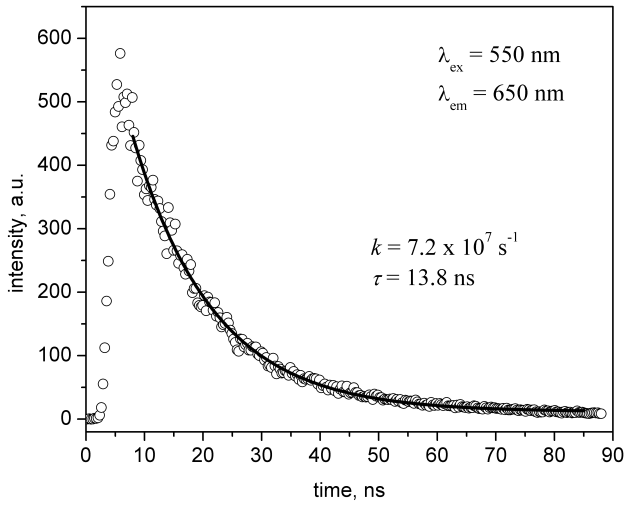


**Fig. S11** The time-decay profile of **2HP** ($9.6 \times 10^{-6}$ M) in PhCN measured by time-resolved fluorescence spectroscopy.

### S3.3. Fitting of data measured by femtosecond laser flash photolysis.

Figures S12–S18 show in their leftmost frames the observed femtosecond time-resolved transient absorption spectra after smoothing and expression on scales linear in frequency and logarithmic in time. Shown in the centre frames are the fits to this data obtained based on kinetics Schemes 2, where R is the unexcited ground-state of the system and the identity of the other product components $P_i$ vary. This

procedure extracts the rate constants $k_i$ and hence the associated reaction times $\tau_i = 1/k_i$, as well as the spectra of each of the product components. The deduced components are shown in the main text in Fig. 4, while the reaction times are given in Table 2. The right-most frames in Figs S12–S18 shows the concentration of each component as a function of time.

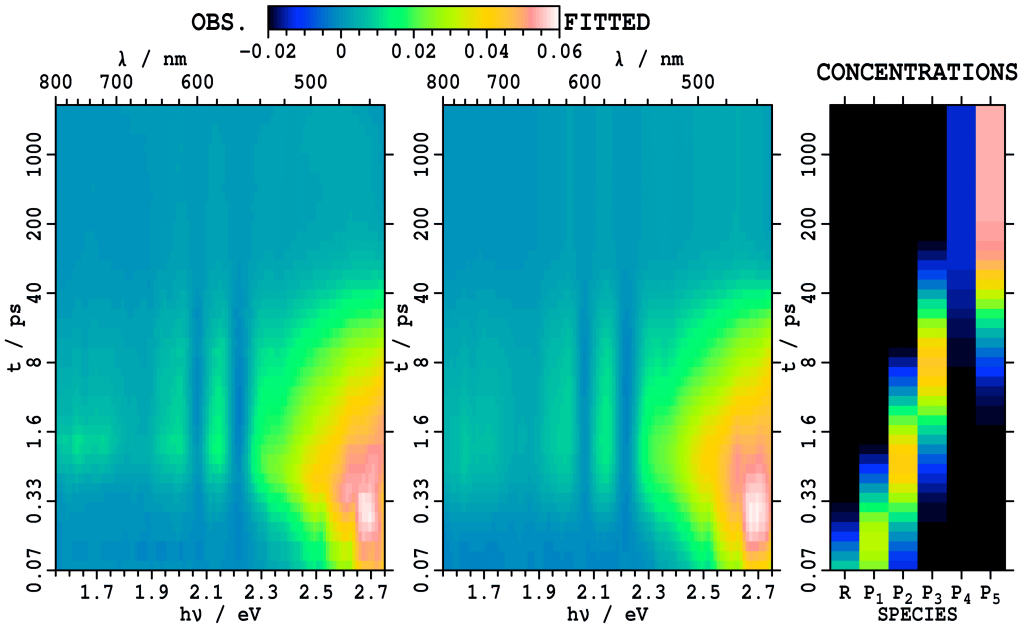


**Fig. S12** Observed and fitted transient absorption spectra following excitation at 430 nm in PhCN at 298 K of **Fc-ZnP** and the concentrations of the reactant R and fitted components $P_1$–$P_5$: $P_1$ is Fc-$^1$ZnP(Soret)$^*$, $P_2$ is Fc-$^1$ZnP($S_1$)$^*$, $P_3$ is $^1$(Fc$^{\bullet+}$-ZnP$^{\bullet-}$), $P_4$ is Fc-$^3$ZnP($T_1$)$^*$, and $P_5$ is the ground state.

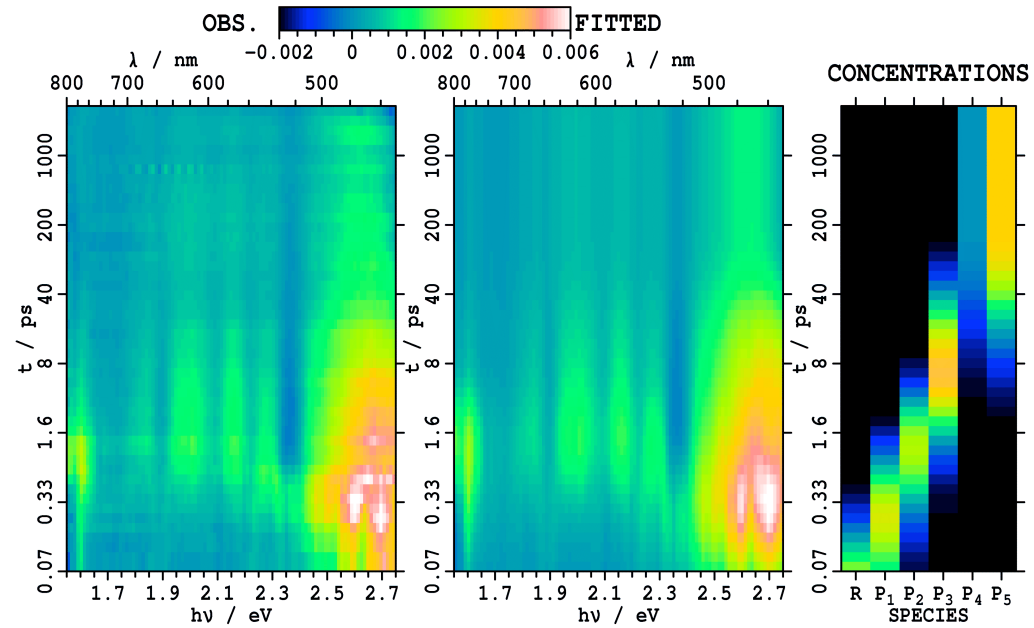


**Fig. S13** Observed and fitted transient absorption spectra following excitation at 430 nm in PhCN at 298 K of **Fc-2HP** and the concentrations of the fitted components $P_1$–$P_5$: $P_1$ is Fc-$^1$2HP(Soret)$^*$, $P_2$ is Fc-$^1$2HP($S_1$)$^*$, $P_3$ is $^1$(Fc$^{\bullet+}$-2HP$^{\bullet-}$), $P_4$ is Fc-$^3$2HP($T_1$)$^*$, and $P_5$ is the ground state.

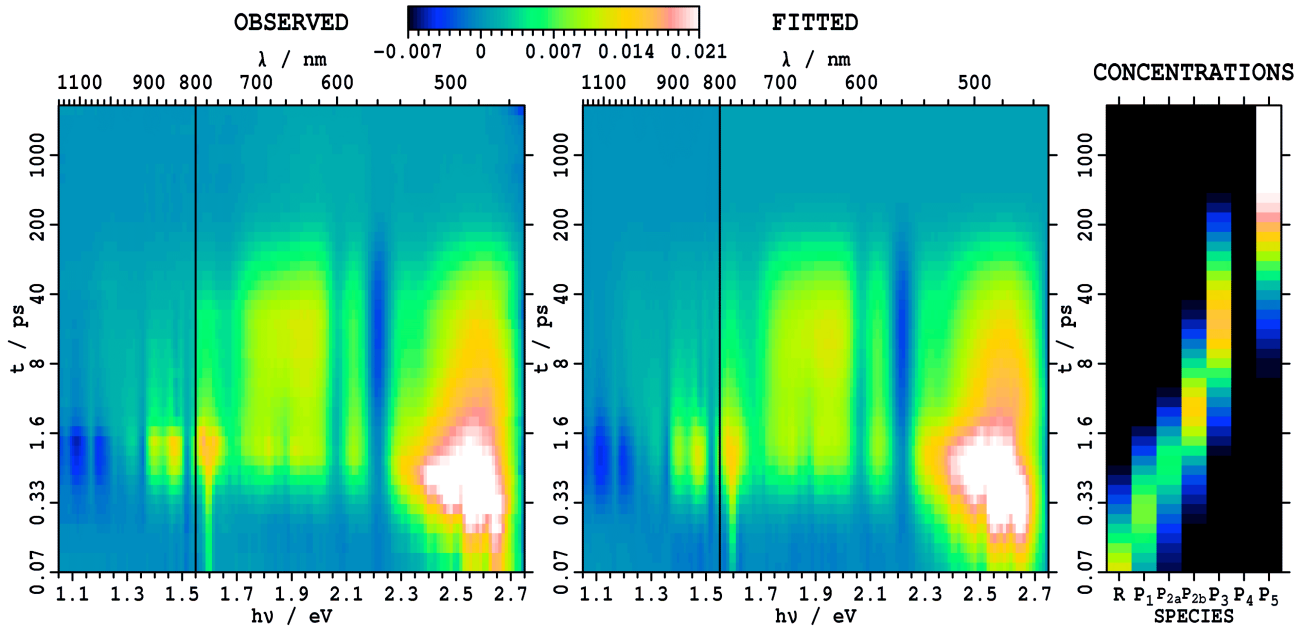


**Fig. S14** Observed and fitted transient absorption spectra following excitation at 430 nm in PhCN at 298 K of **ZnP-C$_{60}$** and the concentrations of the fitted components $P_1$–$P_5$: $P_1$ is $^1$ZnP(Soret)$^*$-$C_{60}$, $P_{2b}$ is $^1$ZnP($S_1$)$^*$-$C_{60}$, $P_3$ is $^1$(ZnP$^{\bullet+}$-$C_{60}^{\bullet-}$), $P_4$ is $^3$(ZnP$^{\bullet+}$-$C_{60}^{\bullet-}$), and $P_5$ is the ground state.

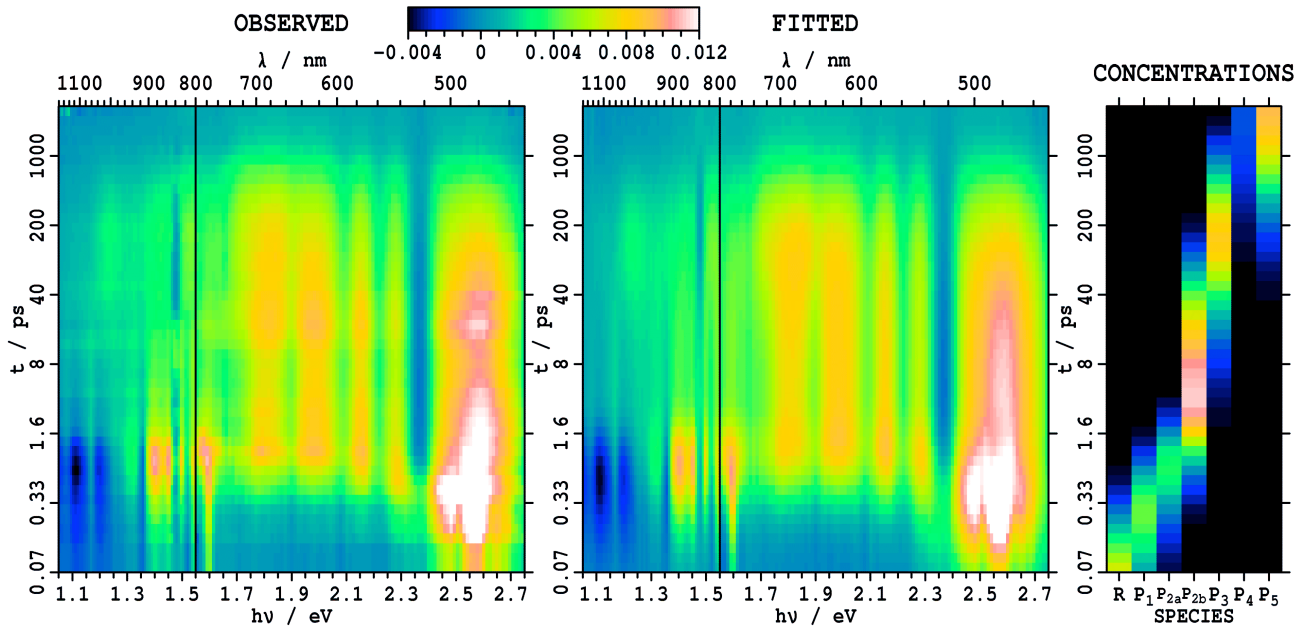


**Fig. S15** Observed and fitted transient absorption spectra following excitation at 430 nm in PhCN at 298 K of **2HP-C$_{60}$** and the concentrations of the fitted components $P_1$–$P_5$: $P_1$ is $^1$2HP(Soret)$^*$-$C_{60}$, $P_{2b}$ is $^1$2HP($S_1$)$^*$-$C_{60}$, $P_3$ is $^1$(2HP$^{\bullet+}$-$C_{60}^{\bullet-}$), $P_4$ is $^3$2HP($T_1$)$^*$-$C_{60}$, and $P_5$ is the ground state.

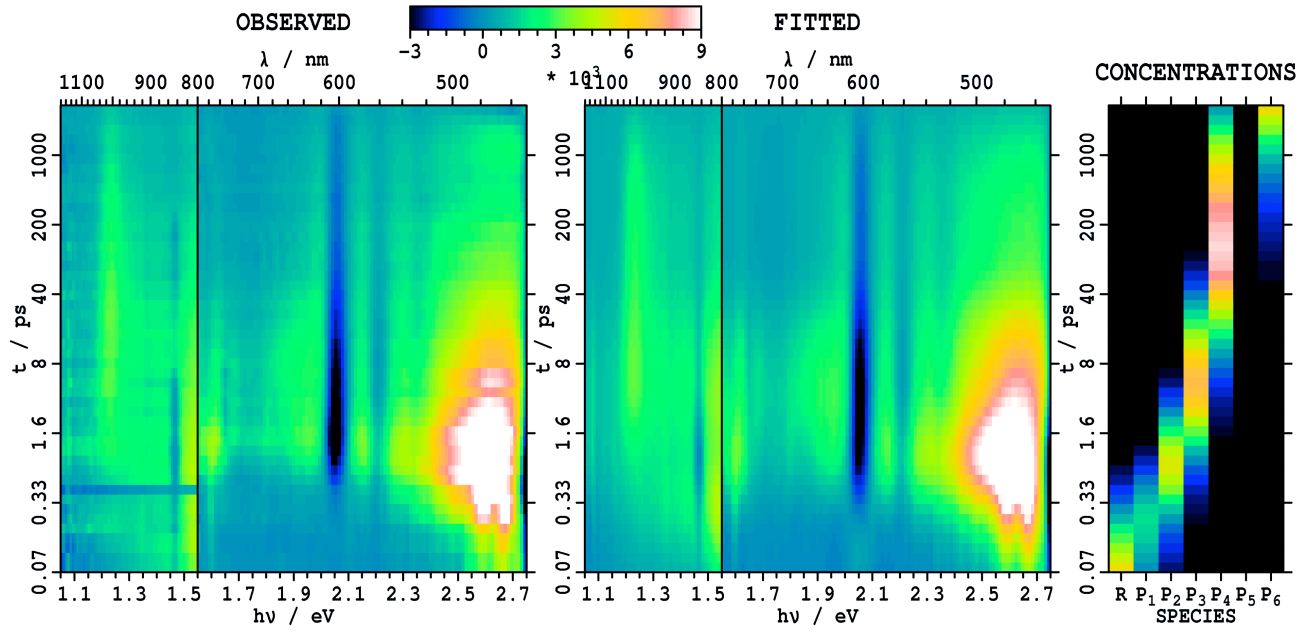


**Fig. S16** Observed and fitted transient absorption spectra following excitation at 430 nm in PhCN at 298 K of **Fc-ZnP-C$_{60}$L** and the concentrations of the fitted components $P_1$–$P_6$: $P_1$ is Fc-$^1$ZnP(Soret)$^*$-$C_{60}$, $P_2$ is Fc-$^1$ZnP($S_1$)$^*$-$C_{60}$, $P_3$ is $^1$(Fc-ZnP$^{\bullet+}$-$C_{60}^{\bullet-}$), $P_4$ is $^1$(Fc$^{\bullet+}$-ZnP-$C_{60}^{\bullet-}$), $P_5$ is $^3$(Fc$^{\bullet+}$-ZnP-$C_{60}^{\bullet-}$), and $P_6$ is the ground state.

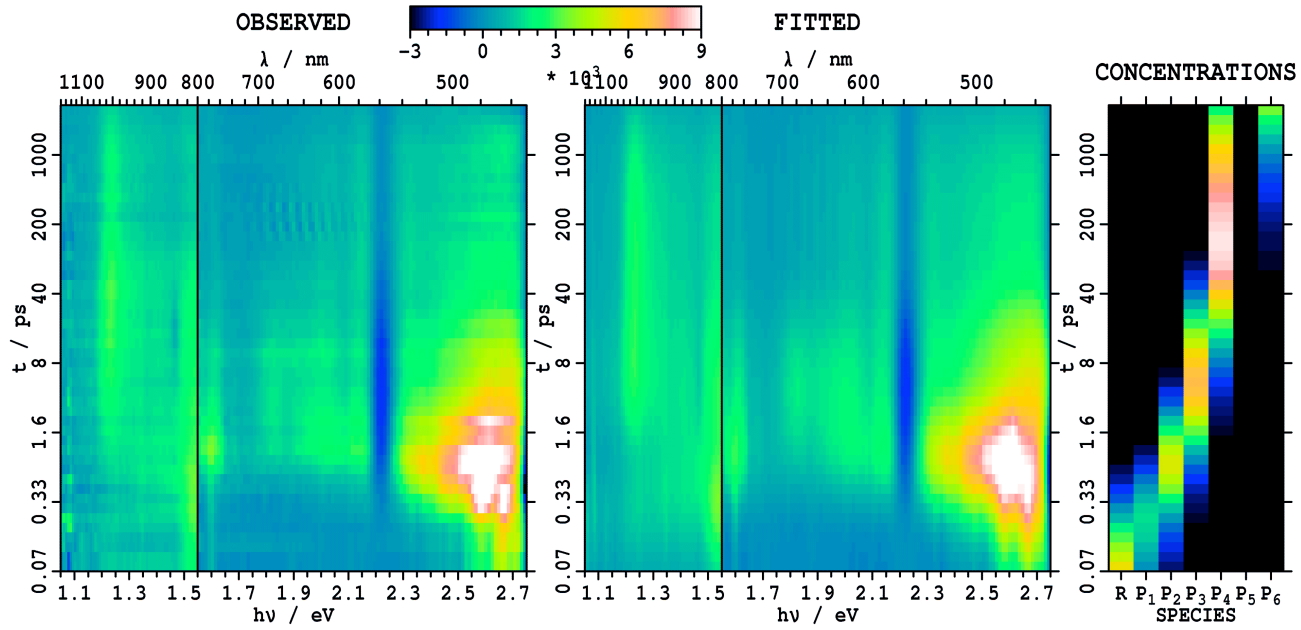


**Fig. S17** Observed and fitted transient absorption spectra following excitation at 430 nm in PhCN at 298 K of **Fc-ZnP-C$_{60}$C** and the concentrations of the fitted components $P_1$–$P_6$: $P_1$ is Fc-$^1$ZnP(Soret)$^*$-$C_{60}$, $P_2$ is Fc-$^1$ZnP($S_1$)$^*$-$C_{60}$, $P_3$ is $^1$(Fc-ZnP$^{\bullet+}$-$C_{60}^{\bullet-}$), $P_4$ is $^1$(Fc$^{\bullet+}$-ZnP-$C_{60}^{\bullet-}$), $P_5$ is $^3$(Fc$^{\bullet+}$-ZnP-$C_{60}^{\bullet-}$), and $P_6$ is the ground state.

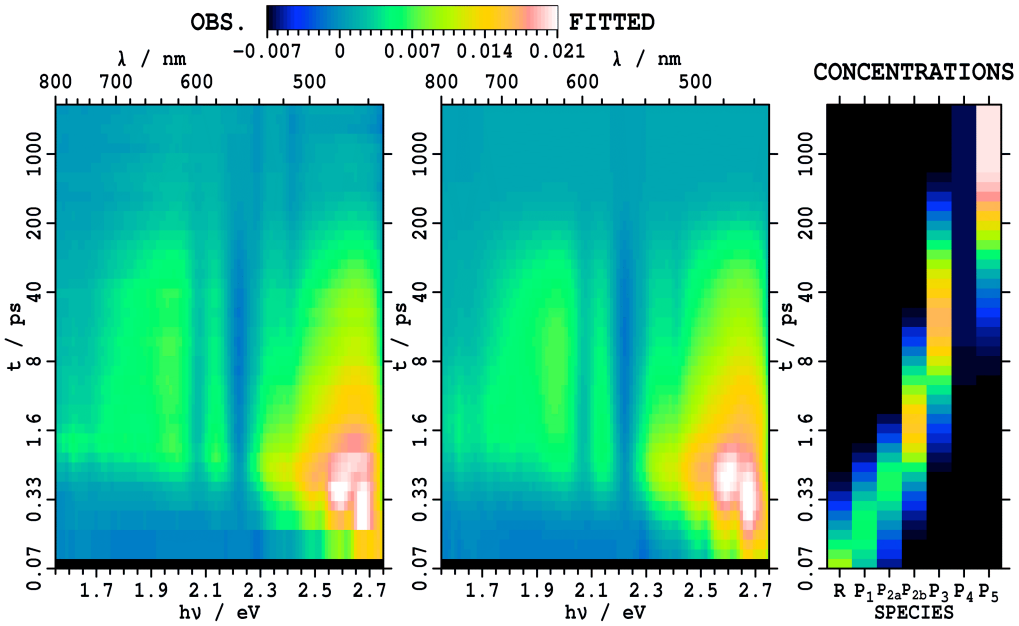


**Fig. S18** Observed and fitted transient absorption spectra following excitation at 430 nm in PhCN containing PhI (0.5 M) at 298 K of **ZnP-C$_{60}$** and the concentrations of the fitted components $P_1$–$P_5$: $P_1$ is $^1$ZnP(Soret)$^*$-$C_{60}$, $P_{2b}$ is $^1$ZnP($S_1$)$^*$-$C_{60}$, $P_3$ is $^1$(ZnP$^{\bullet+}$-$C_{60}^{\bullet-}$), $P_4$ is $^3$(ZnP$^{\bullet+}$-$C_{60}^{\bullet-}$), and $P_5$ is the ground state.

### S3.4. Bimolecular charge-recombination.

Fullerenes and porphyrins can both display strong π-stacking interactions, raising the possibility that solute molecules agglomerate in solution. The meso aryl substituents on the porphyrins keep the planes of adjacent porphyrin molecules well separated from each other in solution, inhibiting this effect. However, the fullerene ball is the correct size to fit inside the aryl groups, making Van der Waals contact with the porphyrin plane. As an example, the gas-phase optimized structure of the dimer of **Fc-ZnP-C$_{60}$L** is shown in Fig. S20. Calculated using Mϕller-Plessett perturbation theory (MP2), the interaction strength between a single $C_{60}$ and a prophyrin is predicted[32] to be 27 kcal mol$^{-1}$. We find that, for the dimer of **ZnP-C$_{60}$**, the two interactions are additive giving a net MP2 binding energy of 55 kcal mol$^{-1}$. Solvent interactions in solution oppose this interaction by 40 kcal mol$^{-1}$ evaluated using B3LYP with a COSMO reaction field, but the resulting calculated net interaction is strong enough to induce complete dimerization even at the low concentration of ca. $4 \times 10^{-5}$ M used in most experiments. MP2 overestimates porphyrin-fullerene interactions significantly,[32] however, and previous photochemical experiments involving tetramesoaryl porphyrins mixed with fullerenes have reported linear dependences of signal on laser excitation power, implying no dimerization. As those experiments cannot discriminate against a scenario in which dimerization is 100% complete, we perform an extensive series of experiments to investigate all possible scenarios.

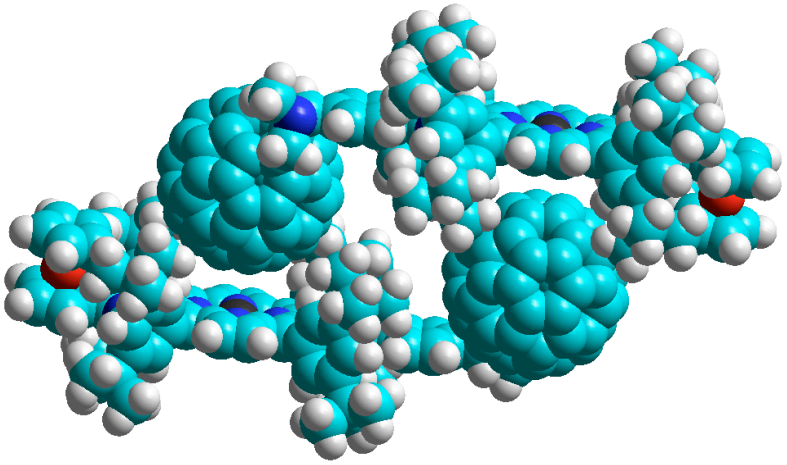

**Fig. S20** B3LYP/3-21G optimized structure of the gas-phase dimer of **Fc-ZnP-C$_{60}$L**; Fe- red, Zn- black, C-cyan, N- blue, H- white.

### S3.4.1. NMR studies of dimerization

To investigate the extent of dimerization expected for this class of molecules in PhCN solution at room temperature, the $^1$H NMR study of **2HP-C$_{60}$** was measured over the range of $2 \times 10^{-5}$ M to $2 \times 10^{-2}$ M in d$_8$-toluene and the results are shown in Figure S21. The results clearly show that at concentrations of $2 \times 10^{-3}$ M and higher the signals from the porphyrin inner NH (~ -2 ppm), the *tert*-butylphenyl protons (1.3–1.7 ppm), the pyrrolidine ring protons (3.2-4.7 ppm) and porphyrin pyrrolic rings protons (7.8–9.2 ppm) are significantly shifted. These changes in NMR signals are due to the close porphyrin/fullerene contact. The dimerization isotherm was fitted to a self-association binding model[31] based on the following chemical equation:

$$2\mathrm{H} \underset{}{\overset{k_\mathrm{d}}{\rightleftharpoons}} \mathrm{H_2} \qquad k_\mathrm{d} = \frac{[\mathrm{H_2}]}{[\mathrm{H}]^2} \tag{S9}$$

For $^1$H NMR dilution study, the following expressions were used to estimate the association constant, $k_\mathrm{d}$,

$$[\mathrm{H_2}] = \frac{1 + 4k_\mathrm{d}[\mathrm{H}]_0 - \sqrt{1 + 8k_\mathrm{d}[\mathrm{H}]_0}}{8k_\mathrm{d}} \tag{S10}$$

$$[\mathrm{H}] = [\mathrm{H}]_0 - 2[\mathrm{H_2}] \tag{S11}$$

$$\delta_{obs} = \frac{2[\mathrm{H_2}]}{[\mathrm{H}]_0}\delta_{\mathrm{H_2}} + \frac{[\mathrm{H}]}{[\mathrm{H}]_0}\delta_{\mathrm{H}} \tag{S12}$$

The association constant of dimerization were ranging from 30–300 M$^{-1}$ (Fig. S22) which is comparable to that of just a single TPP/C$_{60}$ interaction (k$_d$ = 100 M$^{-1}$).[49] This suggests that there is a strong anti-cooperative effect associated with the dimerization of the bichromophoric species, perhaps associated with the additional excluded volume that is apparent from Fig. S21. This result indicates that dimerization is very weak at $10^{-5}$–$10^{-6}$ M concentrations used in the photochemical experiments.

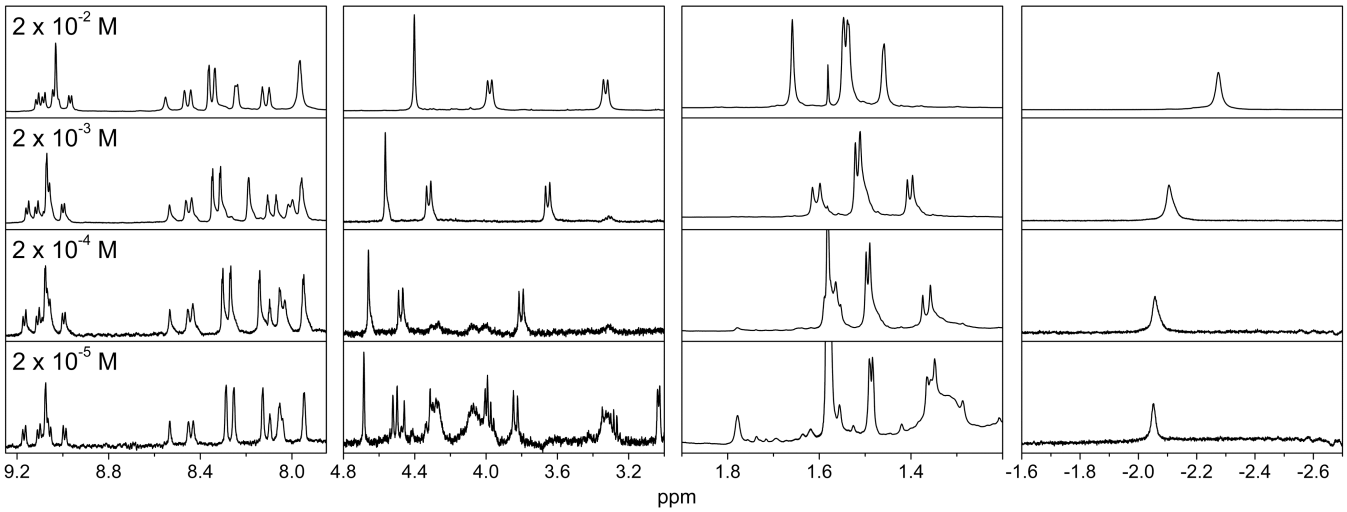


**Fig. S21** The $^1$H NMR study of **2HP-C$_{60}$** at different concentrations in d$_8$-toluene.

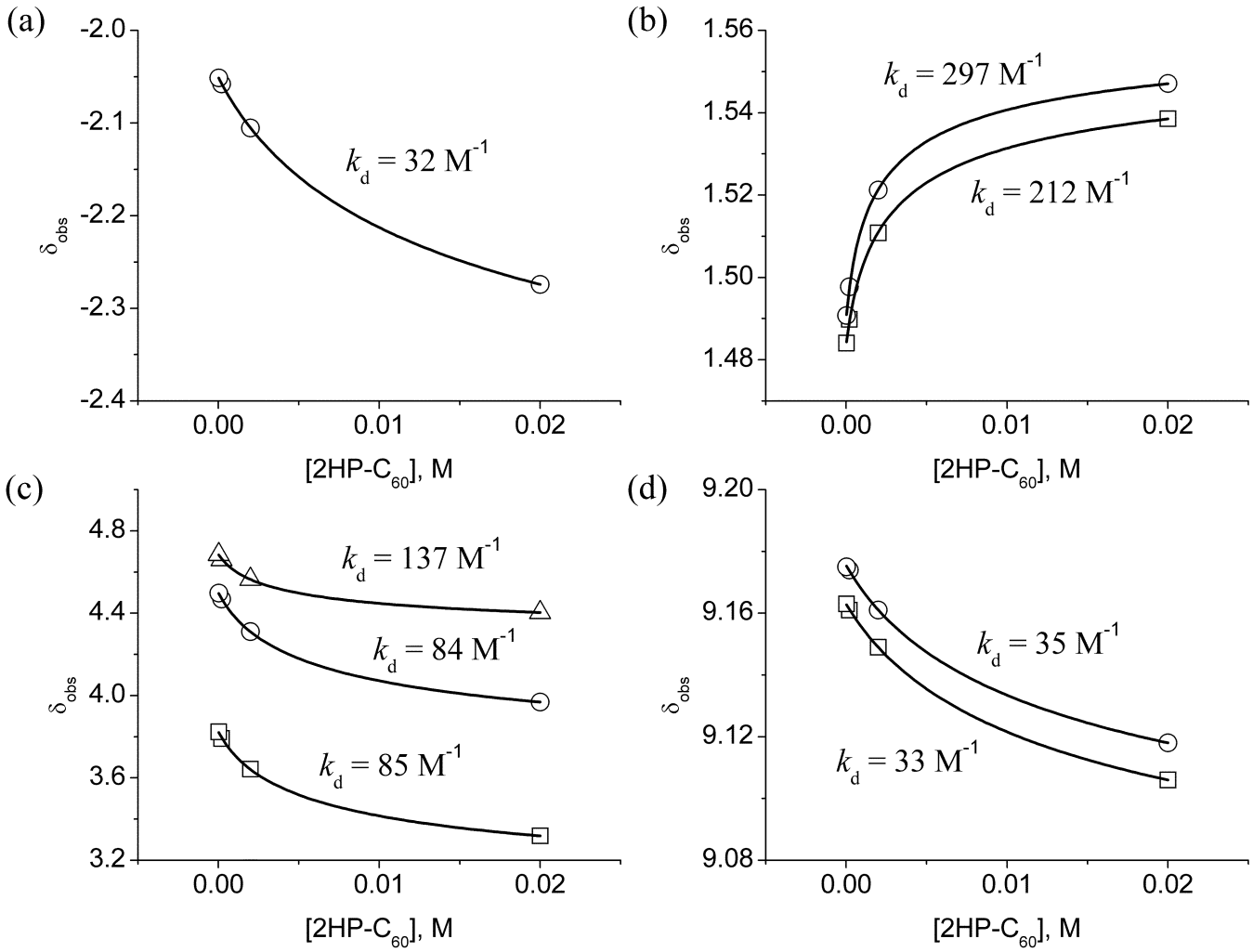


**Fig. S22** The $^1$H NMR isotherms of di-*tert*-butylphenyl protons in **2HP-C$_{60}$** at different concentrations in $d_8$-toluene.

### S3.4b. Concentration dependence of the NIR charge-transfer absorption of ZnP-C$_{60}$.

Vis-NIR absorption spectroscopic study of **ZnP-C$_{60}$** was carried out over the range of 1 × 10$^{-5}$ M to 1 × 10$^{-4}$ M in toluene and Fig. S23 shows the spectra between 500 nm and 1100 nm. The broad signal observes at 840 nm can be indentified as an intramolecular charge-transfer (CT) absorption band[40-42] because of the linear dependence of the intensity of CT band with the concentration of **ZnP-C$_{60}$** (Fig. S23 inset). The emission study shows another linear relationship of the intensity of fluorescence signal with concentrations of different model systems (Fig. S25). It is possible that a small concentration of dimers could dominate the observed photochemistry, but these results demonstrate that the intramolecular interactions remain paramount.

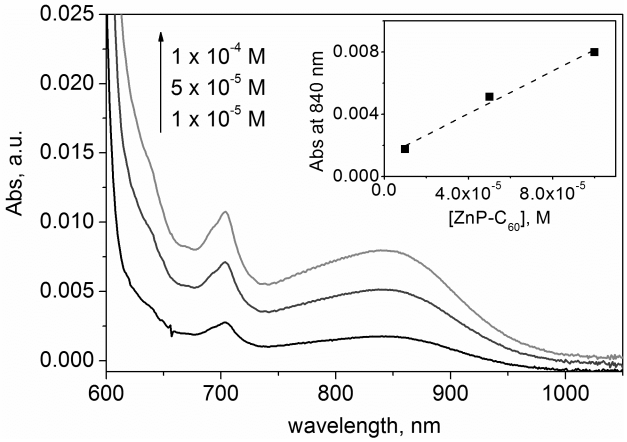


**Fig. S23** Vis-NIR absorption spectra of **ZnP-C$_{60}$** at different concentrations in toluene and the plot of **ZnP-C$_{60}$** concentration against absorbance at 840 nm (inset); absorbance scale in arbitrary units.

### S3.4.3. Concentration dependence of singlet emission.

Figure S24 shows sample emission spectra of **2HP-C$_{60}$** observed as a function of concentration from $10^{-8}$–$10^{-3}$ M, spanning from a noise-limited response to a region in which the emission increases regularly with concentration to a region of strong fluorescence quenching, presumably associated with short-range excitonic interactions. The most crucial region is $10^{-7}$–$10^{-5}$ M for which a linear relationship between log intensity and log concentration is revealed for **2HP-C$_{60}$**, **ZnP-C$_{60}$**, **Fc-ZnP-C$_{60}$L** and **Fc-ZnP-C$_{60}$C** in Fig. S25. The slope of these regions varies between 0.81 and 0.87, with a slope of 1 expected in an essentially all-monomer region and a slope of 0.5 expected in an all-dimer region, assuming that dimers do not fluoresce. While the observed slopes indicate that the solution is essentially un-dimerized before excitation, the deviation of the slopes from the expected value, the possibility of unidentified processes is raised.

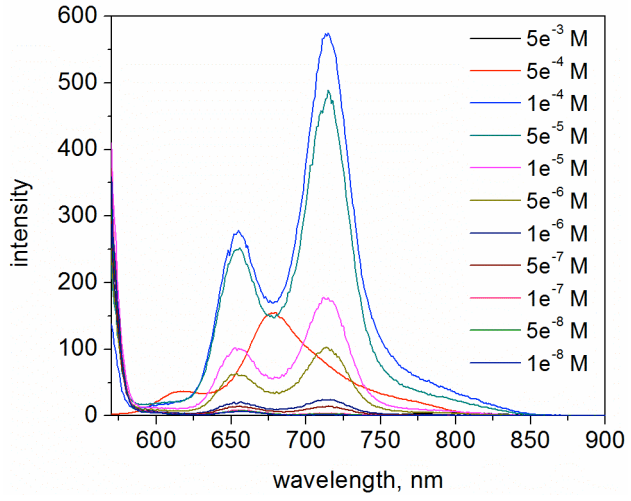


**Fig. S24** Emission spectra of **2HP-C$_{60}$** at different concentrations in cyclohexane following excitation at 555 nm.

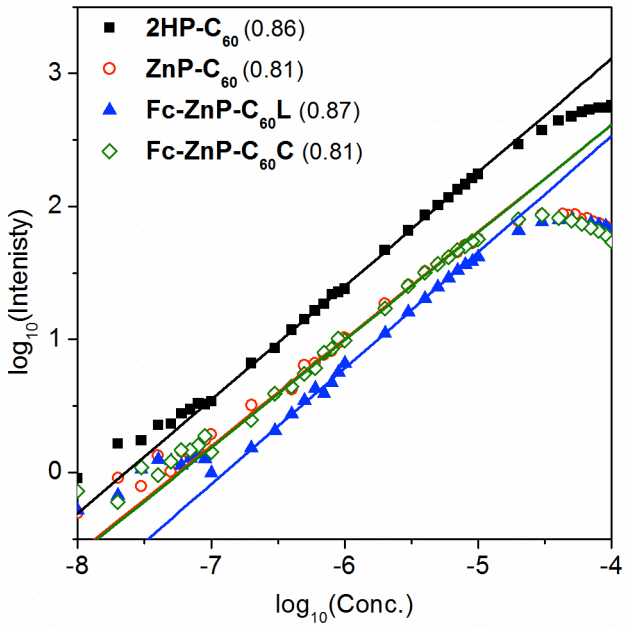


**Fig. S25** The plot of concentrations of **2HP-C$_{60}$**, **ZnP-C$_{60}$**, **Fc-ZnP-C$_{60}$L** and **Fc-ZnP-C$_{60}$C** against the emission intensity in cyclohexane following excitation at 555 nm, in the brackets are the slopes of the linear fittings.

### S3.4.4. Concentration dependence of charge recombination kinetics.

While dimerization does not occur before excitation, the dimerization energy will be significantly enhanced for the exciplex between an excited molecule and a ground-state molecule, and enhanced significantly for the exciplex formed between two excited molecules, either before or after charge separation. For **ZnP-C$_{60}$**, **Fc-ZnP-C$_{60}$L**, and **Fc-ZnP-C$_{60}$C**, double-exponential nanosecond transient decays were observed (see main text Fig. 4).

The concentration dependence in charge recombination (CR) of **ZnP-C$_{60}$** is shown in Fig. S26, with the associated exponential fits presented in Table S2. At the high concentration of 4 × $10^{-5}$ M (used for main text Fig. 4), two distinct exponential components are observed with lifetimes of 120 ns and 660 ns; the short component accounts for 25% of the decay. At the lowest concentrations of 2 × $10^{-6}$ M and 6 × $10^{-6}$ M, only the long-lived component is apparent, however. At the intermediate concentration of 1 × $10^{-5}$ M, a third long-lived component of ca. 3700 ns is also apparent, complicating the analysis. Evidence is found of a weak fast component, however. The results indicate that the fast component goes away at low concentration and hence can be assigned as to a bimolecular exciplex recombination.

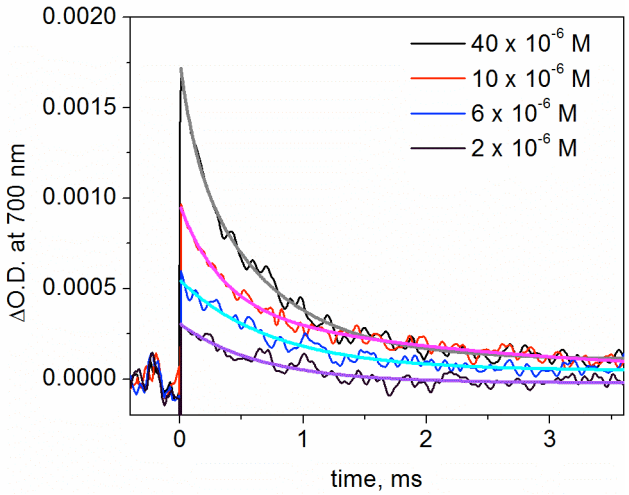


**Fig. S26** The time decay profile of optical density at 700 nm following nanosecond laser flash pulse irradiation of vary concentrations of **ZnP-C$_{60}$** at 355 nm in PhCN at 298 K. The raw data is smoothed using Gaussian convolution at a resolution of 20 $\mu$s.

**Table S2** Fast (bimolecular) and slow (unimolecular) decay charge-recombination processes extracted from the observed nanosecond transient absorption spectra of **ZnP-C$_{60}$** after excitation at 355 nm in PhCN at 298 K

| [**ZnP-C$_{60}$**] | % Bimolecular CR | $\tau_{\text{Bimolecular CR}}$ ($\mu$s) | $\tau_{\text{Unimolecular CR}}$ ($\mu$s) |
|---|---|---|---|
| 40 × $10^{-6}$ M | 25 | 120 | 660 |
| 10 × $10^{-6}$ M | 15 | 100[a] | 490[a] |
| 6 × $10^{-6}$ M | 0 | - | 760 |
| 2 × $10^{-6}$ M | 0 | - | 650 |

[a] A third long-time component is also found of lifetime 3700 ns. The signal to noise ratio is insufficient to allow for an authoritative 3-component analysis, however, and so these results are only provisional. An alternative analysis is to ignore least significant component, the fast one, altogether. This gives 340 ns for the main component and 2500 ns for the slow one. Hence the tree-component analysis appears to make more physical sense then does this simpler approach.

### S3.4.5. Laser-power dependence of charge recombination kinetics.

The concentration-dependence studies reported in Section S4d do not discriminate between dimers formed between one or two excited species, however, and the light transmission is high and hence increasing the concentration increases the concentration of both excited and non-excited species. So exciplex formation is also investigated by monitoring the laser-power dependence of the nanosecond transient decay and the results are given in Fig. S27 and Table S3. At high laser power both the fast and slow components are discernable but the fast component fades at low laser power. This indicates that the bimolecular complex forms between two molecules in their excited states.

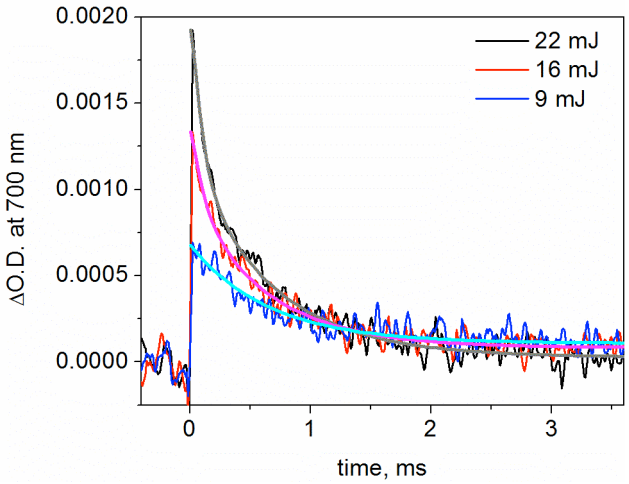


**Fig. S27** The time decay profile of optical density at 700 nm following vary power of nanosecond laser flash pulse irradiation of **ZnP-C$_{60}$** at 355 nm of 3 × 10$^{-5}$ M in PhCN at 298 K.

**Table S3** Fast (bimolecular) and slow (unimolecular) decay charge-recombination processes extracted from the observed nanosecond transient absorption spectra of **ZnP-C$_{60}$** (3 × 10$^{-5}$ M) after excitation at 355 nm in PhCN at 298 K

| Laser power (mJ) | % Bimolecular CR | $\tau_{\text{Bimolecular CR}}$ ($\mu$s) | $\tau_{\text{Unimolecular CR}}$ ($\mu$s) |
|---|---|---|---|
| 22 | 47 | 90 | 667 |
| 16 | 35 | 103 | 630 |
| 9 | 0 | - | 656 |

## S3.5. Hole transfer from excited fullerenes.

In Fig. S28 the observed emission spectra at the same concentration from the zinc porphyrin dyad and the two triads are shown. The emission from the porphyrin S1 state (dominating the 610 nm and 655 nm emissions) is quenched even more in the triads than that it is in the dyad, qualitatively supporting the charge-separation lifetimes reported in Table 2 of the main text. The emission peaks at 476 nm and 496 nm (dominated by fullerene emission) are also quenched but to a lesser extent. This shows that hole transfer from the fullerene does contribute to the photocurrent but its magnitude is too small to be properly identified in the transient absorption spectra.

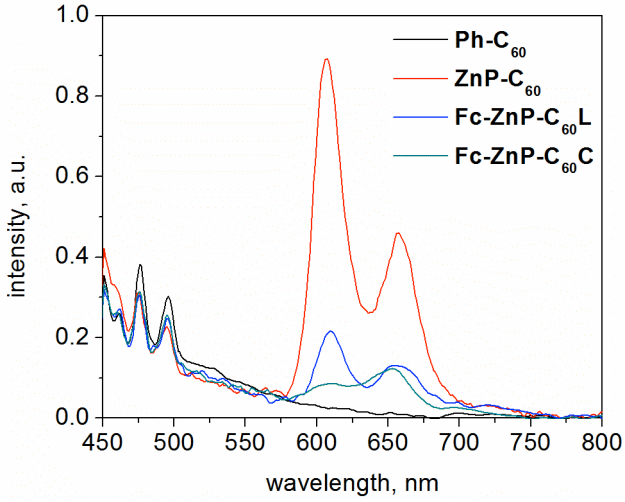


**Fig. S28** Emission spectra of **Ph-$C_{60}$**, **ZnP-$C_{60}$**, **Fc-ZnP-$C_{60}$L** and **Fc-ZnP-$C_{60}$C** ($1 \times 10^{-6}$ M) with excitation wavelength at 430 nm in PhCN at 295 K.

## S3.6. Vibrational parameters deduced for the molecular fragments from B3LYP vibrational frequency analysis.

B3LYP calculations are performed for the neutral and ionized forms of the porphyrin, fullerene, and ferrocene fragments. These fragments include the neighbouring joining groups such as imidazole and phenyl rings. The total intramolecular reorganization energy $\lambda_i$ is determined from the difference in total electronic energy between the vertically excited and equilibrium structures of the ions. These are then partitioned into contributions from the normal modes by curvilinear projection. Only the modes with large displacement are included in the calculations, with the displacement of these modes renormalized so as to preserve the total intramolecular reorganization energy. The included mode frequencies and dimensionless displacements are given in Table S4.

**Table S4** Vibrational parameters used in the determination of Franck-Condon factors for charge-transfer processes[a]

| Mode | Fc-$Fc^+$ ($\lambda_i$ = 0.114 eV) | | P-$P^{\bullet+}$ ($\lambda_i$ = 0.036 eV) | | $C_{60}$-$C_{60}^{\bullet-}$ ($\lambda_i$ = 0.116 eV) | |
|---|---|---|---|---|---|---|
| | Freq. | Displ. | Freq. | Displ. | Freq. | Displ. |
| 1 | 172 | 1.862 | 44 | 1.401 | 149 | 1.280 |
| 2 | 212 | 0.966 | 76 | 1.683 | 650 | 0.546 |
| 3 | 217 | 1.211 | 1454 | 0.230 | 1233 | 0.460 |
| 4 | 242 | 0.996 | 1556 | 0.297 | 1408 | 0.680 |
| 5 | 257 | 1.011 | | | 1477 | 0.415 |
| 6 | 335 | 0.991 | | | 1524 | 0.393 |
| 7 | 640 | 0.664 | | | | |

[a] The vibration frequencies are in $cm^{-1}$ while dimensionless displacements are given. The Huang-Rhys factor S is given by $(displacement)^2/2$.

## S3.7. $^1$H NMR spectroscopy.

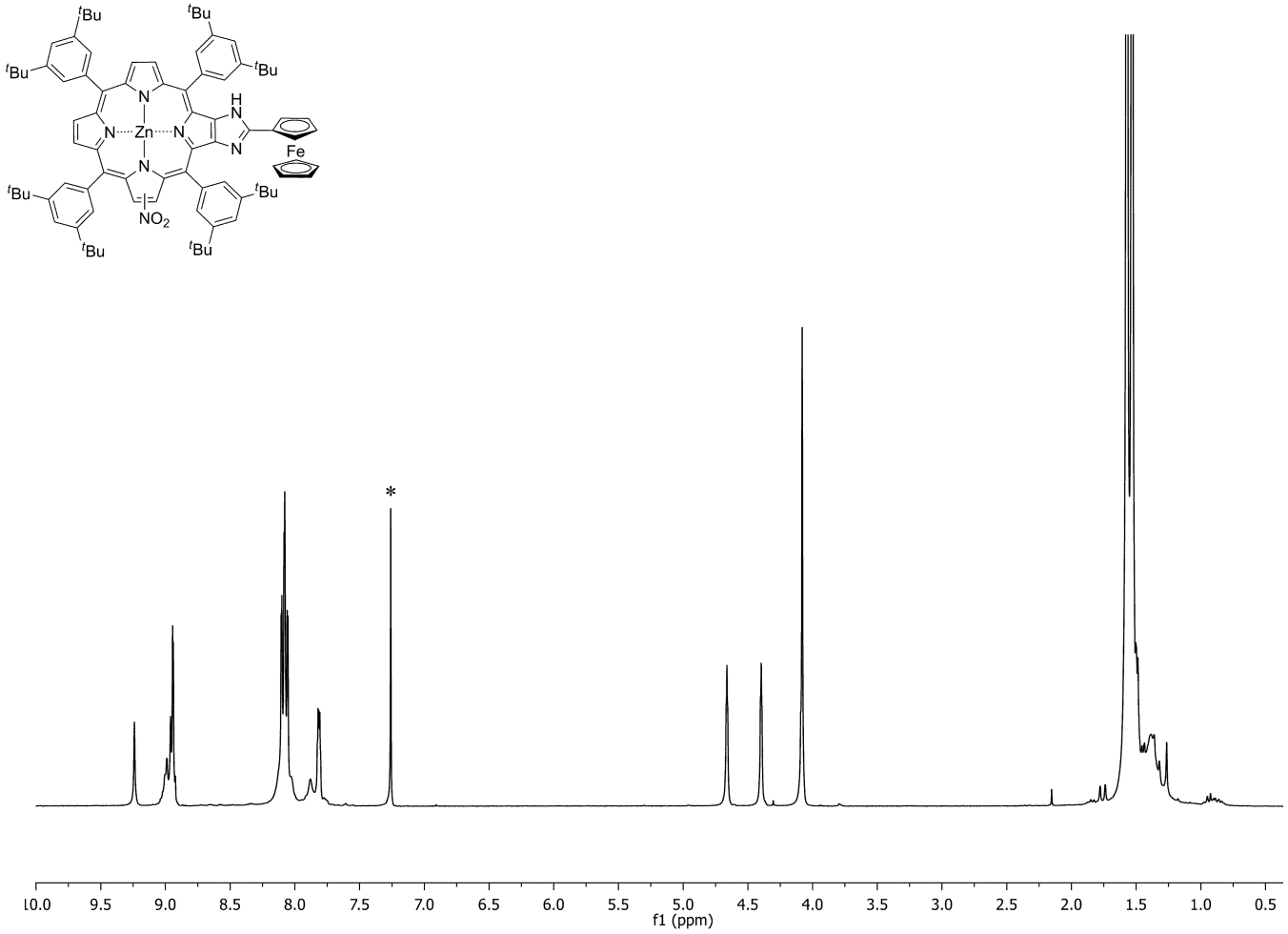


**Fig. S29** $^1$H NMR spectrum (300 MHz, $CDCl_3$) of ferrocene-nitro-(zinc porphyrin) **2**.

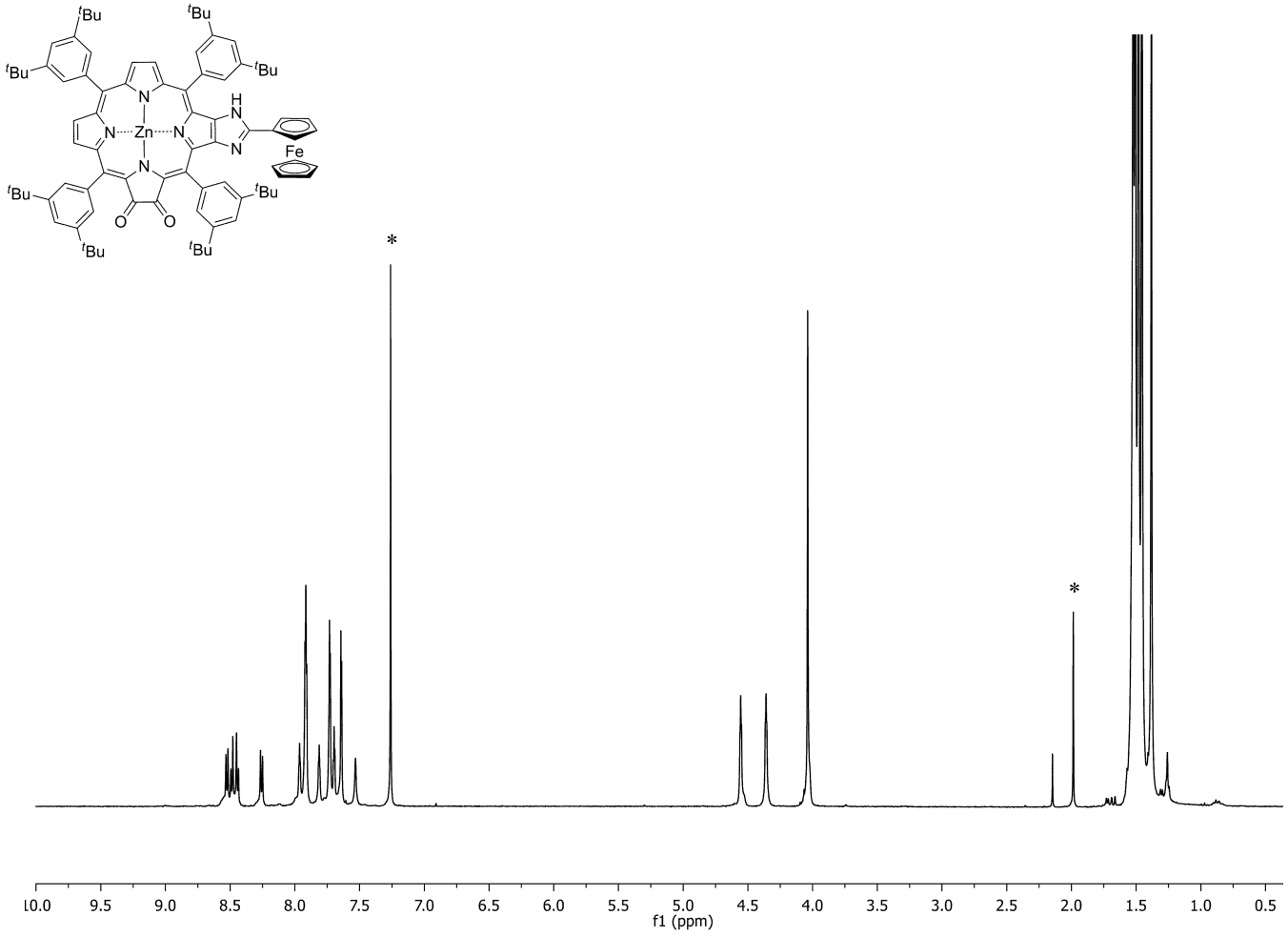


**Fig. S30** $^{1}$H NMR spectrum (300 MHz, $CDCl_3$) of ferrocene-zinc porphyrin-dione **3**.

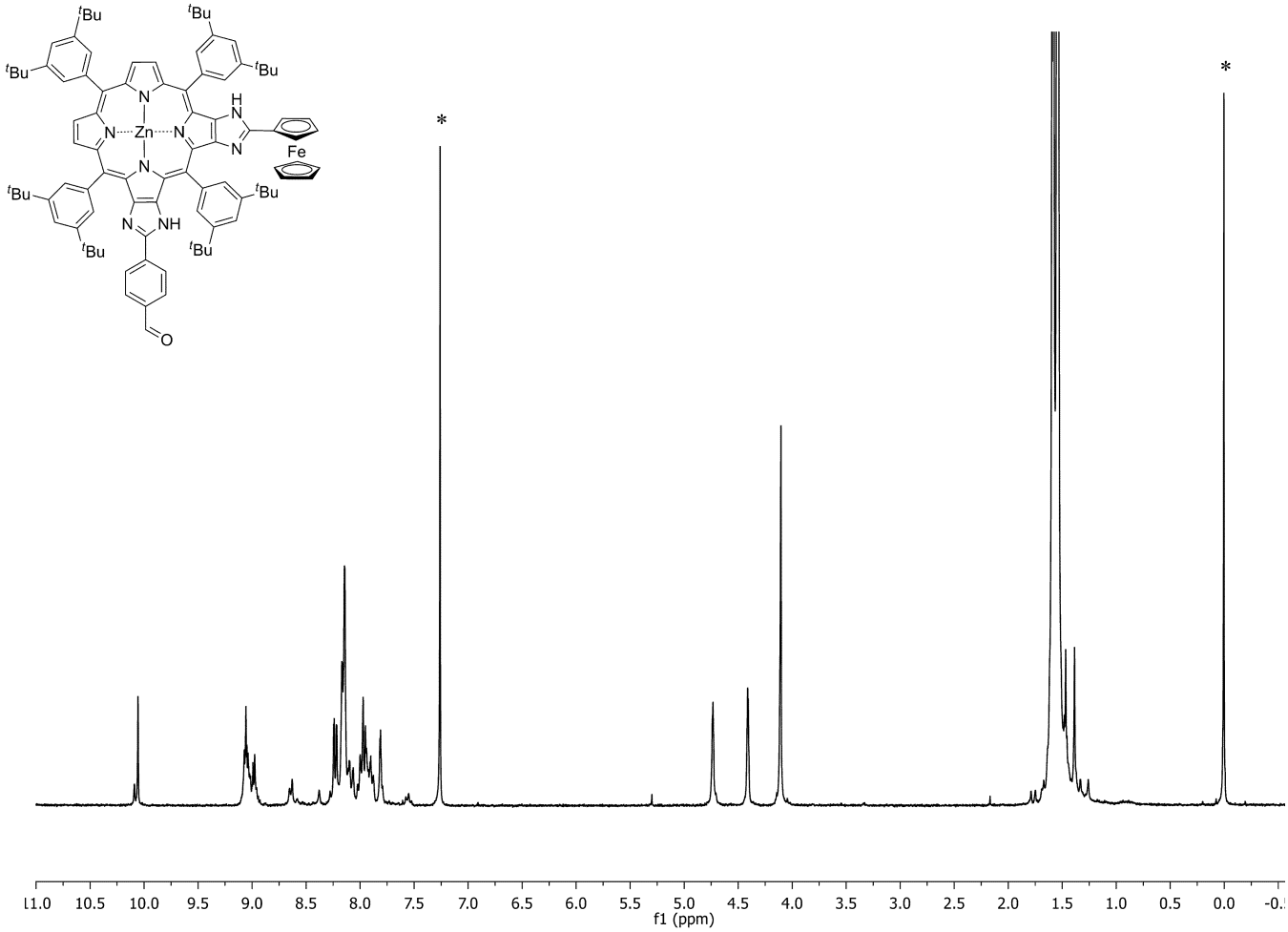


**Fig. S31** $^{1}$H NMR spectrum (300 MHz, $CDCl_3$) of ferrocene-porphyrinoimidazole-benzaldehyde **4**.

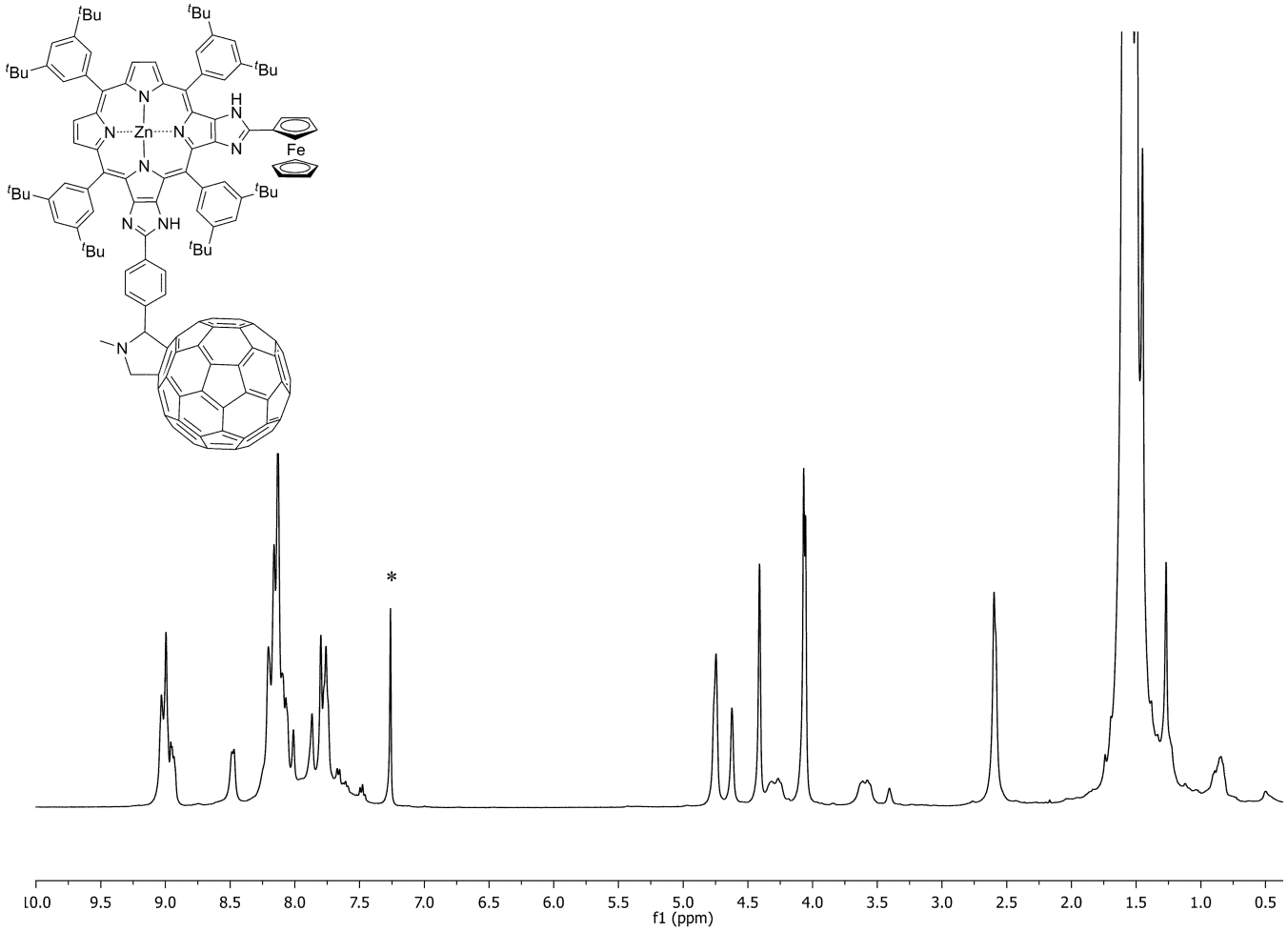


**Fig. S32** $^1$H NMR spectrum (400 MHz, $CDCl_3$) of corner ferrocene-(zinc porphyrin)-fullerene triad **Fc-ZnP-$C_{60}$C**.

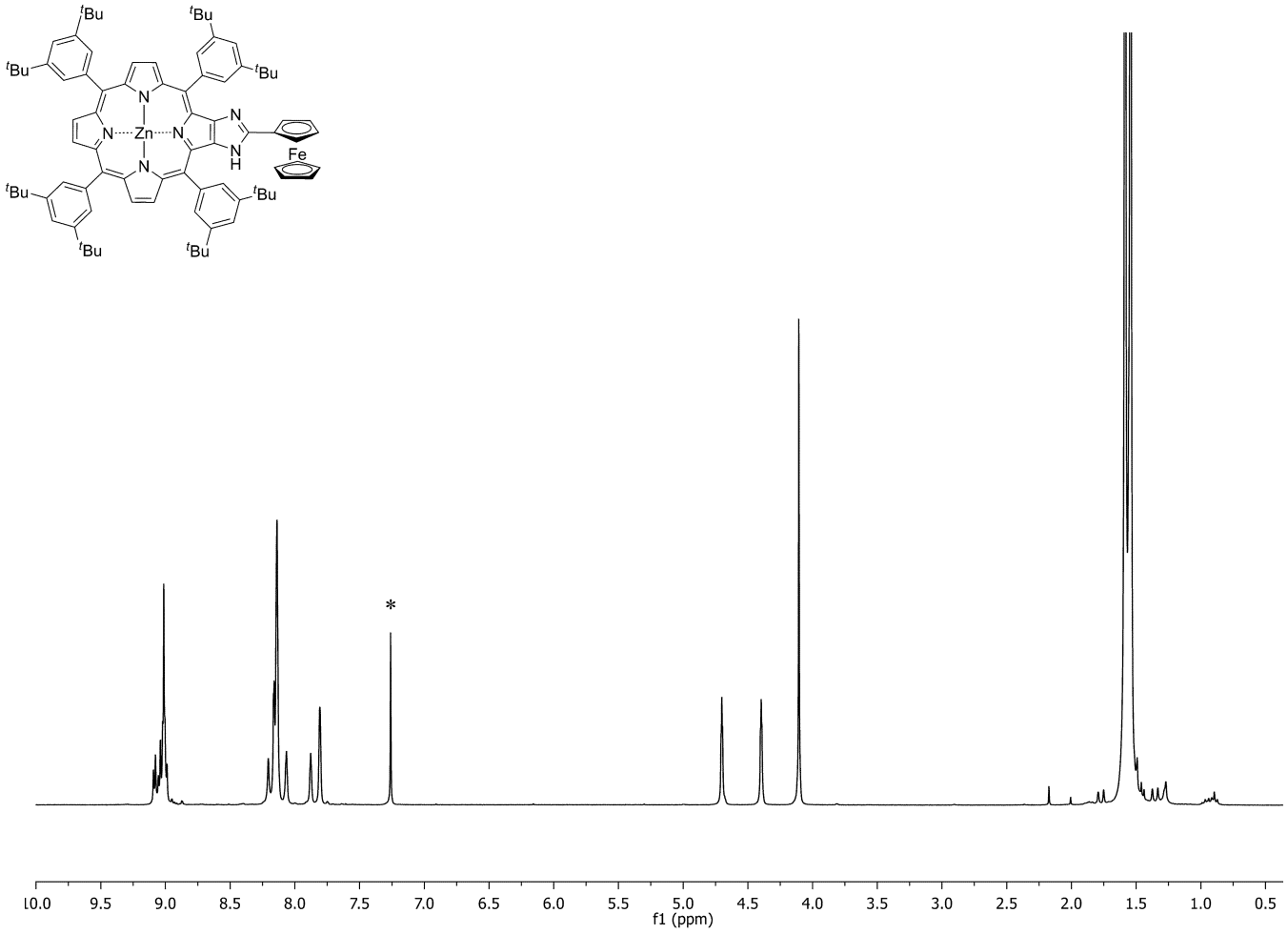


**Fig. S33** $^{1}$H NMR spectrum (300 MHz, $CDCl_3$) of ferrocene-(zinc porphyrin) dyad **Fc-ZnP**.

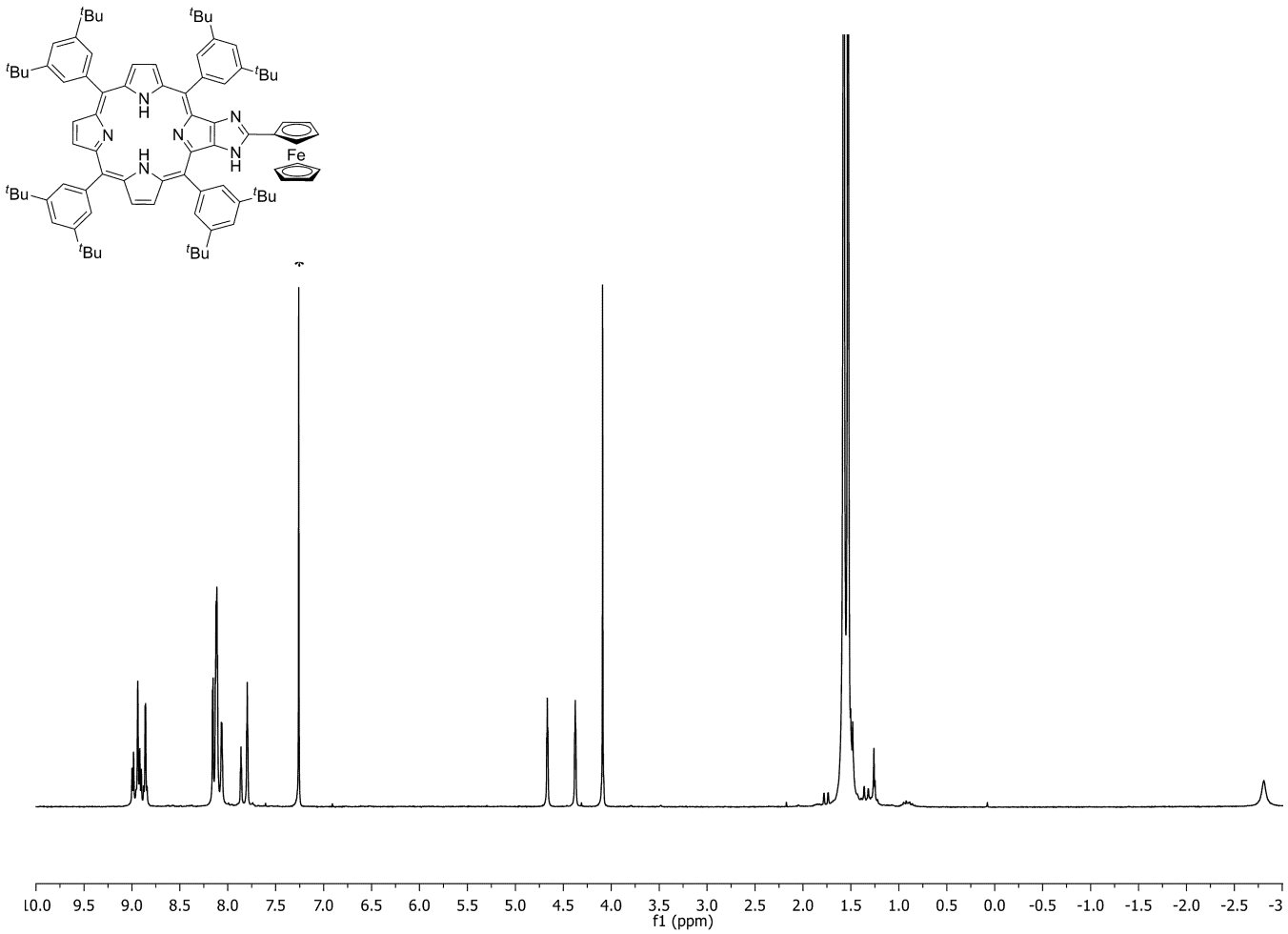


**Fig. S34** $^{1}$H NMR spectrum (300 MHz, $CDCl_3$) of ferrocene-(free-base porphyrin) dyad **Fc-2HP**.

## S3.8. EPR studies.

Figure S35 shows the EPR spectra of chemically oxidized **ZnP** and **Fc-ZnP** obtained in benzonitrile solutions quenched to 150 K. Similarly treated ferrocene gives no signal under these conditions. The signal observed for **Fc-ZnP** is much weaker than that for **ZnP** and arises through delocalization of the radical centre from the ferrocene to the porphyrin.

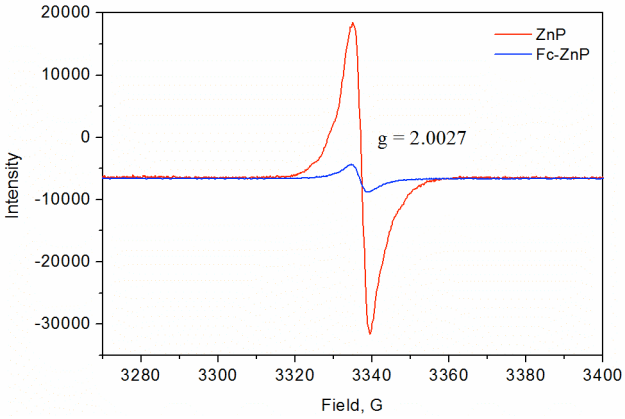


**Fig. S35** Electron-paramagnetic-resonance spectra of **ZnP** and **Fc-ZnP** in 1.0 × $10^{-4}$ M benzonitrile solutions with the presence of iodine (1.0 x $10^{-5}$ M) at 150 K, revealing the presence of $ZnP^{\bullet+}$ (at $g$ = 2.0027).

Figure S36 shows the observed time-decay profiles of the EPR signal strength of **ZnP-$C_{60}$** measured in samples in benzonitrile glasses quenched to 183 K. This displays a single-exponential decay with a lifetimes of 360 s, respectively. The top frames of this figure show the EPR spectra recorded at the initial and final times used for this scan. An Eyring plot investigating the temperature dependence of the decay rate is shown in Fig. S37 and indicates that the reaction probability is extremely low but occurs over a barrier of height 2.0 kcal $mol^{-1}$.

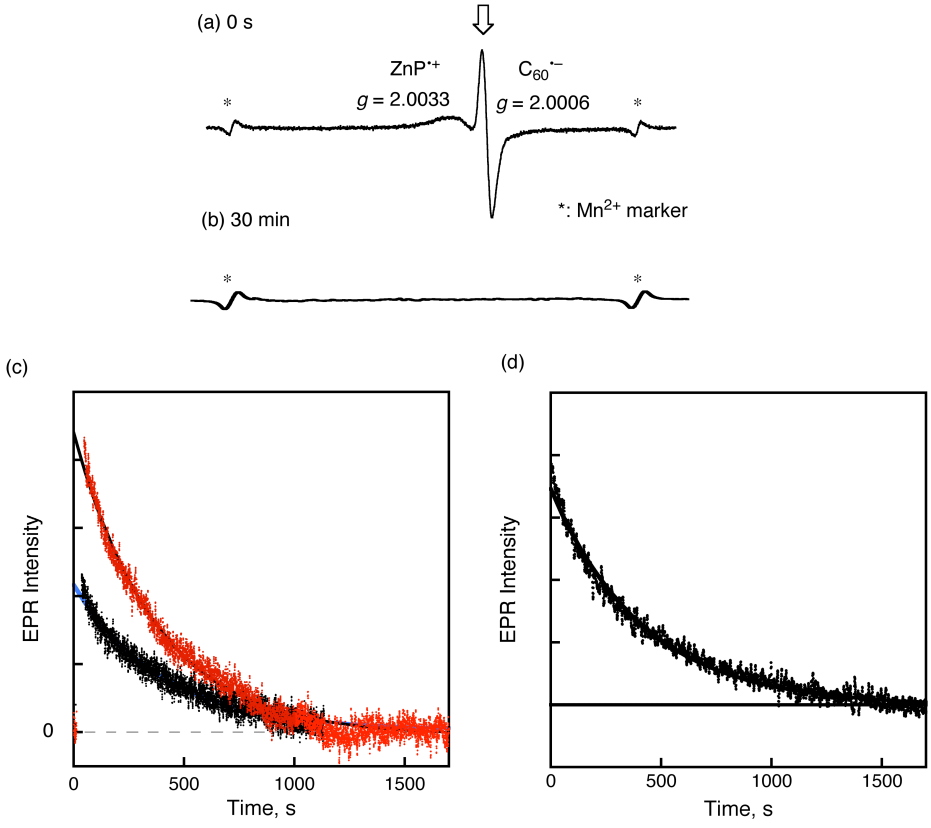


**Fig. S36** EPR spectra of ZnP–$C_{60}$ (2.0 × $10^{-4}$ M) in deaerated PhCN at 223 K after photorradiation at (a) 0 min and (b) 30 min. Light source: a high-pressure mercury lamp with a cut-off filter ($\lambda$ < 430 nm). (c,d) Decay time profile of EPR signal due to the $C_{60}^{\bullet-}$ moiety of the CS state, measured using different concentrations of the CS state. In (c), the concentration is fixed at 2.0 × $10^{-4}$ M and the photoirradiation time is varied by a factor of two, while in (d) the concentration is reduced to 5.0 × $10^{-5}$ M; for each set of results, solid lines are drawn representing a single-exponential decay at $\tau$ = 360 s.

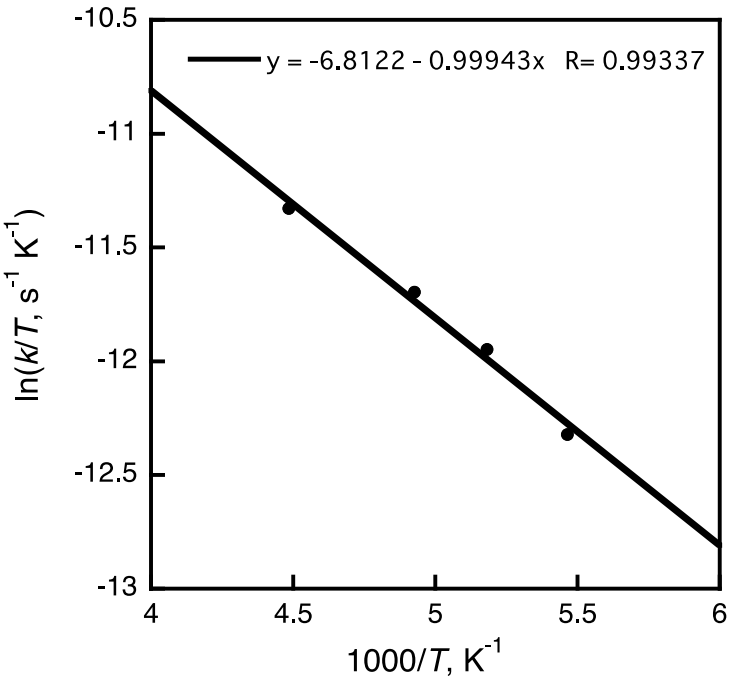


**Fig. S37** Eyring plot of the dependence of the rate constant for decay of the EPR signal of **ZnP-C$_{60}$** at 2.0 x $10^{-4}$ M concentration in benzonitrile glass as a function of inverse temperature.